



Fabrication, surface engineering and applications of new materials

Edited by Santosh K. Tiwari, Yogendra Kumar Mishra,
Oluwafunmilola Ola and Ganesh Chandra Nayak

Imprint

Beilstein Journal of Nanotechnology
www.bjnano.org
ISSN 2190-4286
Email: journals-support@beilstein-institut.de

The *Beilstein Journal of Nanotechnology* is published by the Beilstein-Institut zur Förderung der Chemischen Wissenschaften.

Beilstein-Institut zur Förderung der
Chemischen Wissenschaften
Trakehner Straße 7–9
60487 Frankfurt am Main
Germany
www.beilstein-institut.de

The copyright to this document as a whole, which is published in the *Beilstein Journal of Nanotechnology*, is held by the Beilstein-Institut zur Förderung der Chemischen Wissenschaften. The copyright to the individual articles in this document is held by the respective authors, subject to a Creative Commons Attribution license.



Structural and magnetic properties of microwave-synthesized reduced graphene oxide/ $\text{VO}_2/\text{Fe}_2\text{O}_3$ nanocomposite

Sumanta Sahoo[‡], Ankur Sood[‡] and Sung Soo Han^{*}

Full Research Paper

Open Access

Address:
School of Chemical Engineering, Yeungnam University, 280
Daehak-ro, Gyeongsan 38541, South Korea

Email:
Sung Soo Han^{*} - sshan@yu.ac.kr

^{*} Corresponding author [‡] Equal contributors

Keywords:
 Fe_2O_3 ; magnetism; microwave irradiation; reduced graphene oxide;
 VO_2

Beilstein J. Nanotechnol. **2025**, *16*, 921–932.
<https://doi.org/10.3762/bjnano.16.70>

Received: 26 March 2025

Accepted: 02 June 2025

Published: 20 June 2025

This article is part of the thematic issue "Fabrication, surface engineering and applications of new materials".

Guest Editors: S. K. Tiwari and O. Ola



© 2025 Sahoo et al.; licensee Beilstein-Institut.
License and terms: see end of document.

Abstract

Reduced graphene oxide (rGO)-assisted microwave (MW) synthesis of metal-oxide-based binary and ternary nanocomposites has recently gained considerable research attention. In this context, the current work demonstrates a facile rGO-supported solid-state MW synthetic route for fabricating a ternary nanocomposite of VO_2 , Fe_2O_3 , and rGO. Here, the MW irradiation for 90 s was found to be suitable for the reduction and exfoliation of graphite oxide to form rGO, the reduction of V_2O_5 to form VO_2 , and the formation of Fe_2O_3 from ferrocene. X-ray diffraction and X-ray photoelectron spectroscopy analyses confirm the formation of distinct metal oxides in the presence of rGO. Furthermore, the morphological analysis reveals the deposition of Fe_2O_3 nanoparticles and VO_2 nanorods on the 2D rGO surface. Notably, the ternary composite displayed good magnetic properties for its potential biomedical applications. Overall, this work explores an efficient and cost-effective synthetic approach for developing graphene-based magnetic nanocomposites.

Introduction

Graphene-based materials have been significantly explored in various fields of materials science due to their unique physical and chemical characteristics [1-4]. The special arrangement of carbon materials in a honeycomb fashion enabled this special class of materials to exhibit desirable characteristics, such as enhanced electrical conductivity, higher mechanical strength, elevated surface area, and high thermal and chemical stability. Owing to such improved characteristics, graphene materials, including their derivatives, are broadly explored for miscella-

neous applications, such as energy storage/conversion, EMI shielding, biosensing, optoelectronics, robotics, flexible electronics, paint industries, textile industries, biomedical devices [5-7]. To be specific, the innovation of graphene unlocked a new era in the field of materials science.

The synthetic approaches of graphene materials including graphene quantum dots, graphene oxide, and reduced graphene oxide (rGO) can be categorized into two classes: top-down and

bottom-up processes. The top-down approaches are found to be comparatively simpler and cost-effective compared to the bottom-up processes. Among the top-down approaches, the microwave (MW)-assisted exfoliation process of synthesizing graphene materials and related nanocomposites (NCs) has gained noteworthy research attention in recent times [8,9]. For synthesizing binary and ternary NCs of graphene materials, several conventional approaches, such as sol–gel, hydrothermal/solvothermal, calcination/thermal annealing, chemical vapor deposition, liquid-phase exfoliation, and freeze-drying have been reported. However, the MW-assisted synthetic approaches are found to be superior to these approaches due to lesser time consumption and the lack of sophisticated instrumentation. In this aspect, Kumar et al. demonstrated a facile MW-assisted synthetic route for the perforation and decoration of Pd nanoparticles (NPs) on rGO sheets [10]. The resultant NC displayed its potential for supercapacitor applications. In another work, Mn_3O_4 nanograins-intercalated rGO NC was synthesized through the MW-assisted hydrothermal approach, which showed superior oxygen reduction reaction (ORR) activity [11]. Aside from the oxides, mixed metal sulfides are likewise reported to be combined with graphene by applying MW irradiation for certain time intervals. In this context, Zhang et al. reported the synthesis of Ni-Co sulfide/graphene NC through MW irradiation at a power of 1000 W for 60 s [12]. As a supercapacitor (SC) electrode, the MW-synthesized NC displayed a specific capacitance of 710 F/g.

The MW-assisted approaches have been further explored for the synthesis of binary NCs based on rGO and iron oxides. In one of our earlier reports, such an MW irradiation-based approach was adopted to synthesize $\text{Fe}_2\text{O}_3/\text{rGO}$ NC, using hemin as the precursor. Owing to its 3D network structure, the NC displayed good electrochemical performance as the SC electrode [13]. In another work, Kumar et al. reported the MW-assisted synthesis of $\text{Fe}_3\text{O}_4/\text{rGO}$ NC using FeCl_3 aqueous salt as the precursor [14]. Ferrocene, an Fe-based organometallic compound, was also utilized as the precursor for developing NCs of iron oxide and graphene through the MW route. For example, Kumar et al. demonstrated the MW-assisted rapid synthesis of a ternary NC based on rGO, carbon nanotubes, and Fe_3O_4 NPs, using ferrocene as the Fe-containing precursor [15]. The NC exhibited its potential to be used for EMI shielding applications.

Inspired by previous research findings, the current article aims to produce a ternary NC based on rGO, VO_2 , and Fe_2O_3 using ultrafast MW irradiation. The applied MW irradiation of only 90 s was found to be beneficial for reducing as well as exfoliating graphite oxide to form rGO. At the same time, the approach was also able to convert V_2O_5 to form VO_2 and synthesize Fe_2O_3 from ferrocene. The structure and properties of the

NC were examined through various characterization techniques. Lastly, the magnetic properties of Fe-containing ternary NCs were also evaluated for their possible biomedical applications.

Experimental Materials

Vanadium (V) oxide (V_2O_5) powder and ferrocene were purchased from Alfa Aesar. The other chemicals used for the synthesis of graphite oxide, such as conc. sulfuric acid (H_2SO_4), hydrogen peroxide (H_2O_2), conc. hydrochloric acid (HCl), potassium chlorate (KClO_3), conc. nitric acid (HNO_3), and ethanol were obtained from Duksan Pure Chemicals Co. Ltd. Graphite powder was supplied by Sigma-Aldrich.

Instrumentation and characterization techniques

The “PANalytical, X’Pert-PRO MPD” instrument (Cu $\text{K}\alpha$ line; $\lambda = 1.5406 \text{ \AA}$) was utilized to carry out the XRD analyses of rGO and the NCs. The Raman spectra of rGO and the related NCs were recorded through the “XploRA plus HORIBA” instrument with a laser excitation of 532 nm. Additionally, the surface analysis was performed using X-ray photoelectron spectroscopy measurements (XPS, Thermofisher Scientific) functioning at 12 kV and 6.50 mA using an Al $\text{K}\alpha$. The morphologies and elemental analyses of rGO and the NCs were analyzed through scanning electron microscopy (SEM, Hitachi, S-4800). The structural analysis of these fabricated NCs was examined using high-resolution transmission electron microscopy (HRTEM, FEI Tecnai G2 F20). Furthermore, the magnetic properties of the NCs were evaluated using a vibrating-sample magnetometer (VSM, LakeShore (8604)).

Microwave synthesis of reduced graphene oxide

Following a previous report, graphite powder was initially oxidized to form graphite oxide to synthesize rGO through MW irradiation [16]. In the next step, 200 mg of the graphite oxide was MW irradiated at 700 W for 90 s in a MW oven. It is important to note that the MW process happened in the solid phase. The reduction and exfoliation of graphite oxide to form the rGO occurred through the removal of oxygen functionalities in the gaseous form. It is interesting to note that the obtained rGO material is found to be much lighter than the graphite oxide precursor.

Microwave synthesis of rGO/ VO_2 nanocomposite

The solid-state MW irradiation process was followed to synthesize the GV NC. In a typical process, initially, the graphite oxide (100 mg) was mixed with V_2O_5 powder (100 mg) in a mortar pestle. In the next step, the mixed powder

was MW irradiated at a power of 700 W for 90 s to obtain the GV NC.

Microwave synthesis of rGO/VO₂/Fe₂O₃ nanocomposite

The ternary NC was synthesized following a similar solid-state MW irradiation process. It is important to note that ferrocene was used as the precursor for the iron oxide. In a typical process, graphite oxide (100 mg), V₂O₅ powder (50 mg), and ferrocene (50 mg) were thoroughly mixed in a mortar pestle. Finally, the mixed powder was MW irradiated at a power of 700 W for 90 s to synthesize the ternary GVF.

Results and Discussion

The NC based on rGO, VO₂, and Fe₂O₃ was synthesized through a cost-effective, ultrafast MW route. As shown in Figure 1, the graphite powder was initially oxidized through a chemical synthetic route to form graphite oxide. In the next step, the MW irradiation of constant power for a fixed time duration was applied to form the NC. It is evident that the NCs of Fe₂O₃ and graphene materials are usually synthesized through hydrothermal/solvothermal processes.

In this aspect, a comparative study of a few ternary NCs based on Fe₂O₃ and graphene materials is shown in Table 1. Most of

the reported synthetic processes are composed of multiple steps, are time-consuming, and utilize higher temperatures. Compared to these approaches, the adopted synthetic route has the advantages of less time and energy consumption. Moreover, the solid-state MW irradiation was conducted inside the MW oven at room temperature. Furthermore, most of the reported works are based on synthesizing Fe₂O₃ from Fe-based aqueous salt in liquid phases. In contrast, the current work demonstrates the formation of Fe₂O₃ from a Fe-based organometallic compound, ferrocene.

Herein, the graphite oxide was utilized as an MW susceptor, which deliberately absorbed the MW irradiation and generated heat. The generation of heat was caused by the interaction of oxygen functionalities with the MW irradiation. The produced heat was capable enough for the conversion of V₂O₅ and ferrocene to form the corresponding oxides, which eventually dispersed on the surface of the graphene sheets. In the meantime, the graphite oxide was reduced and exfoliated to form rGO. The oxygen functionalities present in the graphite oxide were partially removed from the reaction system in the form of gases (e.g., CO₂, CO) [25]. On the other hand, the remaining oxygen-containing functional groups on the graphene surface acted as a good support for the attachment of metal oxide NPs on the graphene surface. It is important to note that the resul-

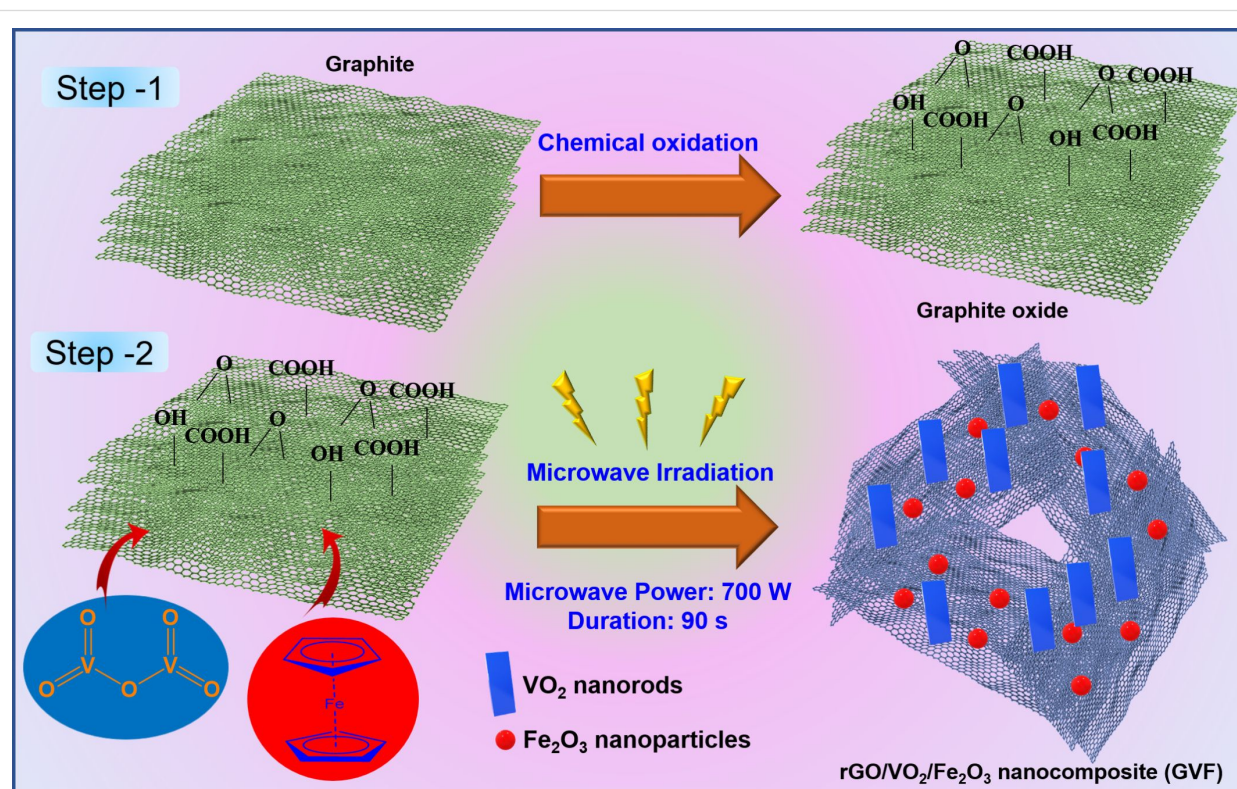


Figure 1: Schematics of the synthetic approach of GVF NC.

Table 1: Comparative study of the reaction conditions of a few ternary NCs based on Fe₂O₃ and rGO.

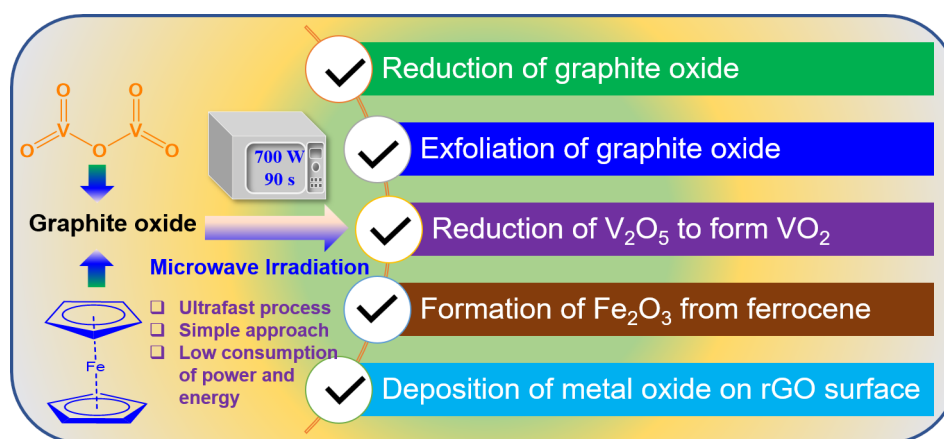
Nanocomposite (NC)	Fe Precursor	Synthetic approach	Conversion time for iron oxide	Conversion temperature for iron oxide	Ref.
graphene/Fe ₂ O ₃ /polyaniline	FeCl ₂ ·4H ₂ O	hydrothermal + in situ polymerization	10 h	180 °C	[17]
rGO/Fe ₂ O ₃ /SnO ₂	FeCl ₃ ·6H ₂ O	hydrothermal + thermal annealing	4 h (hydrothermal) 1 h (thermal annealing)	120 °C 400 °C	[18]
Fe ₂ O ₃ /NiO/rGO	ferric nitrate	hydrothermal + MW heating	5 h (hydrothermal) 10 min (MW)	180 °C 700 °C	[19]
C ₃ N ₄ /Fe ₂ O ₃ /V ₂ O ₅	FeCl ₃ ·6H ₂ O	stirring + hydrothermal + thermal annealing	5 h (stirring) 12 h (hydrothermal) 2 h (annealing)	60 °C (stirring) 160 °C (hydrothermal) 500 °C (annealing)	[20]
C ₃ N ₄ /Fe ₂ O ₃ /graphene aerogel	FeCl ₃ ·6H ₂ O	stirring + hydrothermal + freeze drying	5 h (stirring) 12 h (hydrothermal)	80 °C (stirring) 180 °C (hydrothermal)	[21]
rGO/Fe ₂ O ₃ /polyindole	Fe(NO ₃) ₃ ·9H ₂ O	hydrothermal + MW irradiation	24 h (hydrothermal) 3 min (MW irradiation)	180 °C (hydrothermal)	[22]
C ₃ N ₄ /Ti ₃ C ₂ /Fe ₂ O ₃	FeCl ₃ ·6H ₂ O	solvothermal	12 h	180 °C	[23]
C ₃ N ₄ /Fe ₂ O ₃ /CdS	FeCl ₃ ·6H ₂ O	calcination	4 h	400 °C	[24]
rGO/VO ₂ /Fe ₂ O ₃	ferrocene	MW irradiation	90 s	room temperature	this work

tant rGO was found to be much lighter than the graphite oxide precursor, which can be ascribed to significant exfoliation of the graphite oxide to form the rGO. Figure 2 schematically summarizes the effects of MW irradiation on the mixed powder of graphite oxide and metal oxide precursors.

The short-life MW irradiation was also successful in converting V₂O₅ to VO₂. This type of phase change of this metal oxide is generally implemented through a few approaches, including annealing, sol–gel process, hydrothermal process, vapor transport method. However, such approaches are time consuming

[26–28]. In this context, the ultrafast reduction of V₂O₅ to VO₂ through the MW route is highly beneficial. On the other hand, the formation and dispersion of Fe₂O₃ NPs on the rGO surface through the decomposition of ferrocene followed a similar mechanism, as discussed in a previous report [29]. Upon MW irradiation, the Fe molecules were oxidized to form Fe₂O₃ and deposited on rGO surfaces through substantial interactions.

To confirm the formation of the ternary NC, the XRD analysis of the GVF was performed. As shown in Figure 3a, the characteristic peaks of GVF corresponding to the α phase of Fe₂O₃

**Figure 2:** Schematics representing the effects of MW irradiation on the mixed powder of graphite oxide, V₂O₅, and ferrocene.

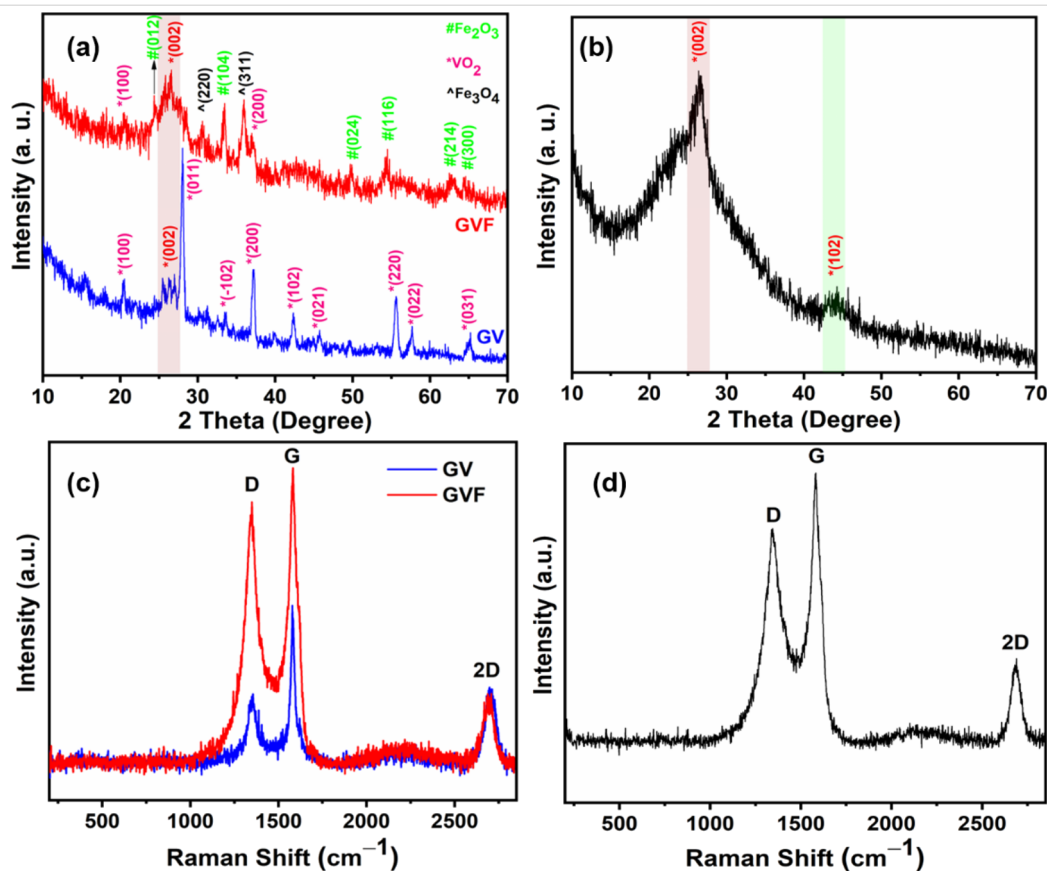


Figure 3: XRD patterns of (a) GV and GVF, (b) rGO; Raman spectra of (c) GV and GVF, and (d) rGO.

and VO₂, along with the signature peak of rGO were observed. To be specific, the peaks at the diffraction angles of 24.4°, 33.5°, 49.8°, 54.4°, 62.8°, and 64.4° indicate the (012), (104), (024), (116), (214), and (300) planes of Fe₂O₃, respectively (JCPDS Card No. 79-0007) [30]. On the other hand, the high-intensity peak at the diffraction angle of 26.5° represents the characteristic (002) plane of rGO. Notably, other high-intensity peaks at $2\theta = 30.6^\circ$ and 36° could be assigned to the (220) and (311) planes of Fe₃O₄, respectively, according to the JCPDS card no. 65-3107 [31]. The presence of such peaks could be accounted for the partial formation of the Fe₃O₄ phase of iron oxide while oxidizing ferrocene alongside Fe₃O₄, which is formed as a major iron oxide component during the MW irradiation process. Nevertheless, the XRD pattern of the GV demonstrates the characteristic peaks of VO₂, according to the JCPDS card no. 01-072-0514 [32]. Specifically, the peaks at the diffraction angle of 20.4°, 28°, 33.5°, 37.2°, 42.3°, 45.8°, 55.5°, 57.6°, and 65.2° can be ascribed to the characteristic (100), (011), ($\bar{1}$ 02), (200), (210), (021), (220), (022), and (031) planes of VO₂. The characteristic peak of the (002) plane of rGO is also exhibited in the diffraction pattern of GV. It is important to note that the diffraction pattern of GVF also displays a few characteristic peaks of VO₂ with smaller intensity values, indicating

its minimal presence in the formed GVF. Additionally, slight shifting of the peak position of individual components in the NCs is an indication of interaction between them. For a comparative study, the XRD pattern of MW-synthesized rGO is shown in Figure 3b. As shown, the high-intensity peak at the diffraction angle of 26.5° corresponds to the (002) plane, and the low-intensity peak at the diffraction angle of 44.2° represents the (102) plane of graphene [33–35]. The presence of rGO in the GV and GVF was further confirmed by the Raman spectra (Figure 3c). As shown, the peaks at ≈ 1350 and ≈ 1580 cm⁻¹ correspond to the characteristic D and G bands of graphene. Interestingly, minor changes in the peak positions of these two characteristic peaks indicate the alteration of the components in the NCs. The formation of defects is a prime characteristic of the MW synthesis of graphene materials. The implementation of MW irradiation generates an enormous amount of heat, which further creates structural defects and disorders in the graphene structure. The intensity ratio of the D and G bands (I_D/I_G ratio) was calculated to evaluate the defects in the NCs. For GV, the I_D/I_G ratio is found to be 0.44. However, the ratio is increased to 0.88 for GVF NC. Such a significant enhancement in the I_D/I_G ratio indicates that the introduction of Fe-based components caused more disorder and defects in the carbon structure

[36]. Furthermore, the peak at $\approx 2700\text{ cm}^{-1}$ represents the characteristic 2D band of graphene. The Raman pattern of rGO represents such characteristic D band at $\approx 1343\text{ cm}^{-1}$, G band at $\approx 1582.4\text{ cm}^{-1}$, and 2D band at $\approx 2690\text{ cm}^{-1}$, respectively (Figure 3d). It is interesting to note that, while GV displays a lower value, GVF displays a higher I_D/I_G ratio than that of rGO (0.79). Notably, the induction of defects in graphene structures through NC formation generally leads to improved magnetic properties [37–39]. Therefore, the GVF is expected to display enhanced magnetic characteristics owing to the induction of higher defects and the presence of $\alpha\text{-Fe}_2\text{O}_3$.

Figure 4a,b represents FESEM images of rGO at low and high magnifications. As shown, the morphological analyses represent the wavy-like networks of rGO nanosheets, demonstrating the exfoliation of graphene sheets. On the other hand, the SEM micrograph of GVF demonstrates the dispersion of the nanorods of VO_2 and NPs on Fe_2O_3 on the graphene surface (Figure 4c,d). It is important to note that the morphological analysis of GVF displays a porous nature, which is also favorable for demonstrating improved magnetic characteristics due to alterations in the electronic structure. To further comprehend the elemental composition of GVF, the elemental analysis was also performed, and the corresponding elemental distribution

and EDX spectrum are shown in Figure 5a,b. The SEM image displays a wide-range distribution of metal oxide components on the graphene surface. Furthermore, the corresponding elemental mapping demonstrates a uniform distribution of C, O, V, and Fe elements, which could be accounted for the presence of VO_2 and iron oxide phases. Additionally, the EDX spectrum also confirms the presence of these elements.

For a comparative study, the morphological analysis of the GV was performed, and the corresponding FESEM images are shown in Figure 6a–c. As shown in the SEM micrographs, at various magnifications, the spherical-shaped VO_2 particles are covered on the graphene surfaces. Notably, such spherical particles of the metal oxides are also deposited on the edges of the graphene sheets (Figure 6d). The corresponding elemental mapping further demonstrates the presence of elements such as V, O, and C in the GV (Figure 6e–h). Additionally, the EDX spectrum also confirms the presence of these elements in the NC (Figure 6i).

Further, to understand the surface electronic arrangement of the elements present in GVF, XPS analysis was performed. Figure 7a represents the survey spectrum, which confirms the presence of V, Fe, and O (derived from the metal oxide counter-

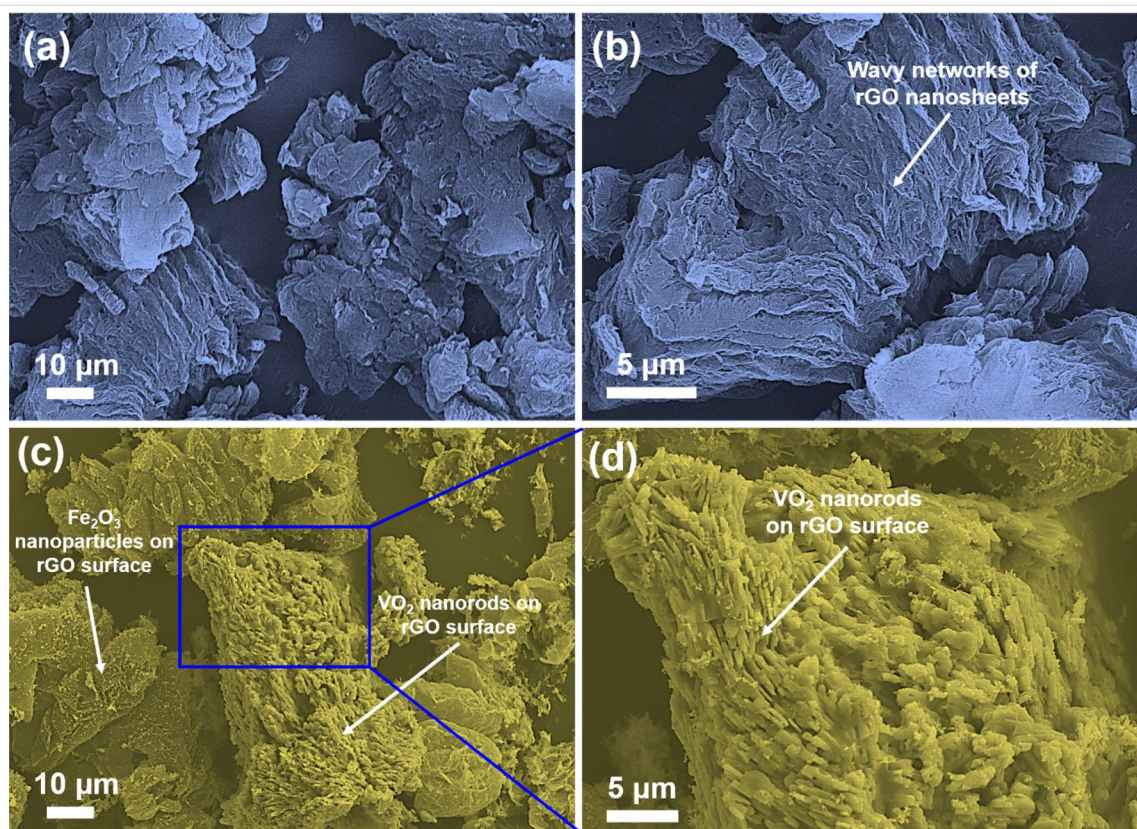


Figure 4: FESEM images of (a, b) rGO and (c, d) GVF NC at lower and higher magnifications.

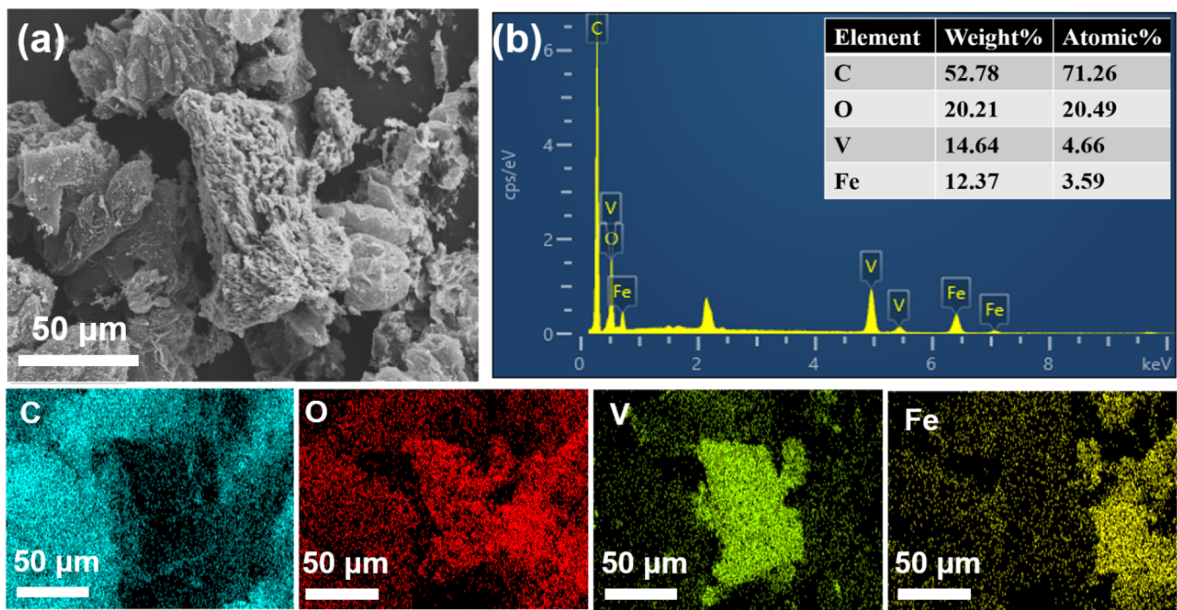


Figure 5: EDX analysis of GVF NC: (a) SEM image (scale bar – 50 μm), (b) EDX spectrum, and the corresponding elemental mapping showing the distribution of C, O, V, and Fe.

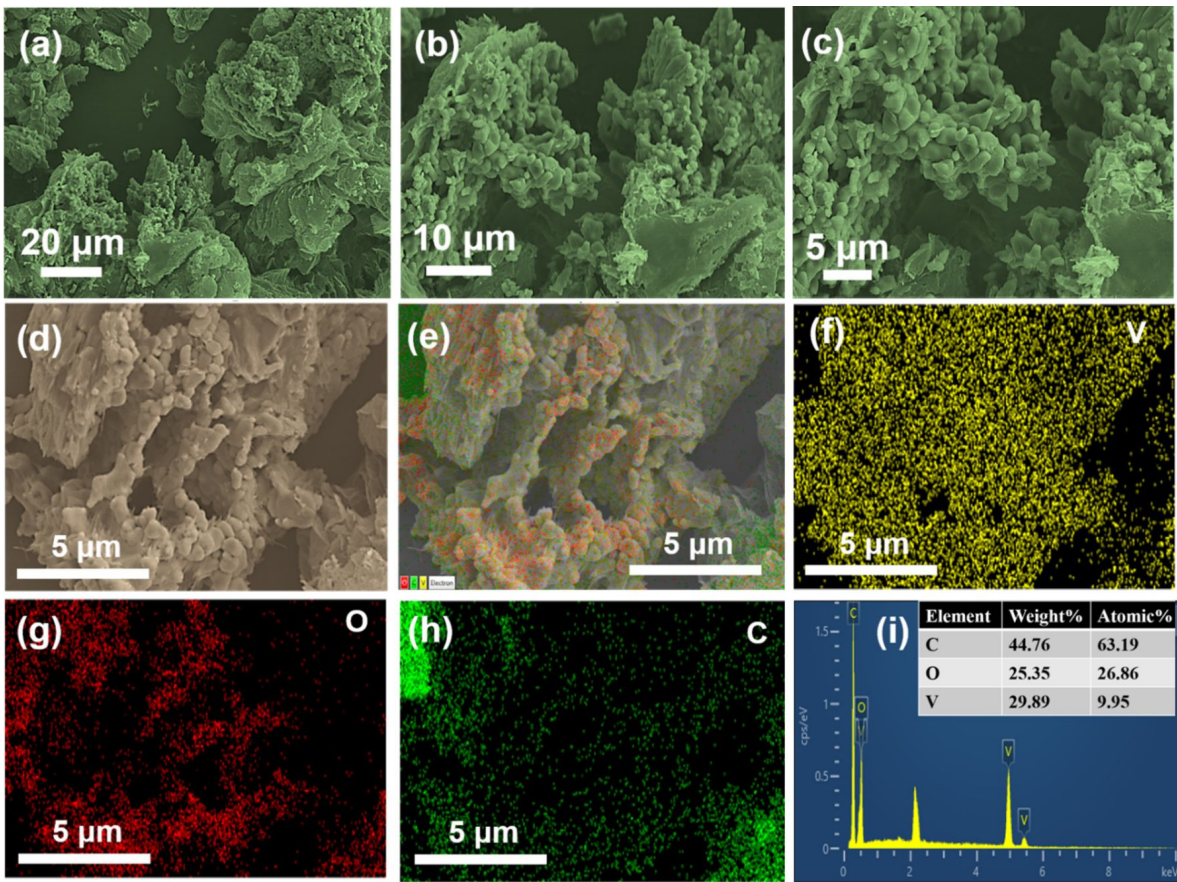


Figure 6: Morphology analysis of GV: (a–c) SEM images at lower and higher magnifications; (d–h) SEM image (scale bar – 5 μm) and corresponding elemental mapping displaying the uniform distribution of V, O, and C elements; (i) EDX spectrum.

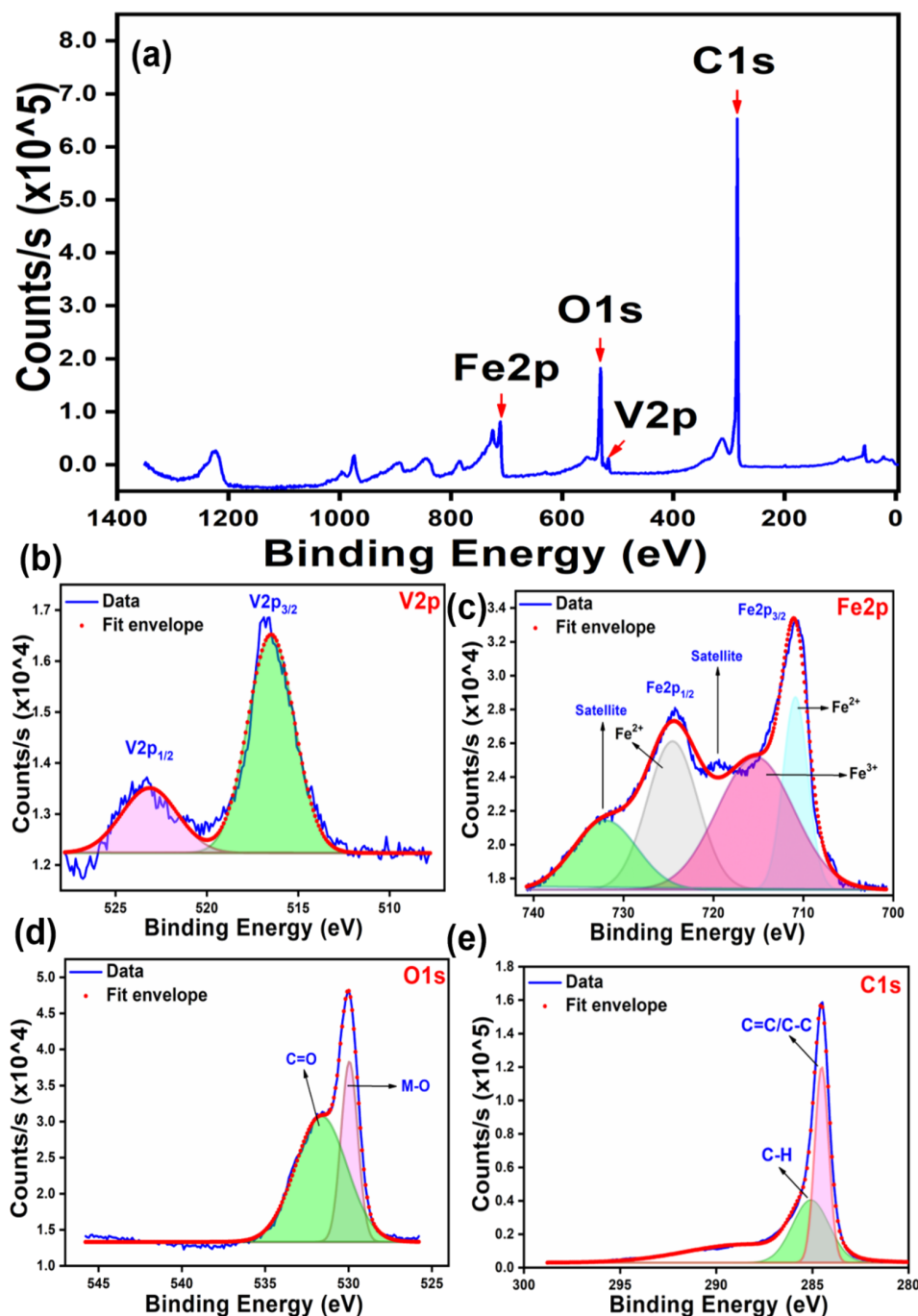


Figure 7: XPS analysis of GVF NC: (a) survey spectrum; high-resolution spectra of (b) V 2p, (c) Fe 2p, (d) O 1s, and (e) C 1s.

parts), along with the C element (derived from rGO). The data thus obtained was in coherence with the reported results from XRD and EDX analysis. Additionally, the high-resolution XPS spectrum of V 2p designates two major peaks at 516.5 and 523.3 eV, which can be ascribed to the V 2p_{3/2} and V 2p_{1/2}, respectively (Figure 7b) [40]. On the other hand, the high-resolu-

tion XPS spectrum of Fe 2p reveals two XPS peaks centered at ≈ 710.8 and ≈ 724.5 eV, which correspond to Fe 2p_{3/2} and Fe 2p_{1/2} levels, respectively (Figure 7c). It is noteworthy to mention that the weak satellite peak at ≈ 719.5 eV indicates the formation of iron oxide in the form of Fe₂O₃, rather than its other counterparts [41]. The deconvolution of O 1s results in the

formation of two major peaks at ≈ 530 and ≈ 531.6 eV (Figure 7d). While the peak at ≈ 530 eV can be designated to the metal–oxygen (M–O) bond, the other peak at ≈ 531.6 eV could be assigned to C=O of rGO. Additionally, the high-resolution XPS spectrum of C 1s represents a major peak at 284.5 eV, corresponding to the C=C/C–C bond, and a minor peak at 284 eV corresponding to the C–H bond of rGO (Figure 7e). Therefore, XPS analysis confirms the presence of distinct metal oxides and rGO in the GVF.

The detailed structure of the GVF was monitored by HRTEM analysis. The corresponding images are shown in Figure 8a–f. As shown in Figure 8a, the rGO nanosheets are found to be transparent and thin in nature. In the magnified HRTEM image, an agglomerated dispersion of Fe_2O_3 NPs and VO_2 nanospheres (NSs) was visible on the thin rGO surfaces. Notably, a clear difference between the size of Fe_2O_3 NPs (average particle diameter – 8.1 ± 2.2 nm) and VO_2 NSs (average particle diameter – 34 ± 5.2 nm) indicates the formation of these two dif-

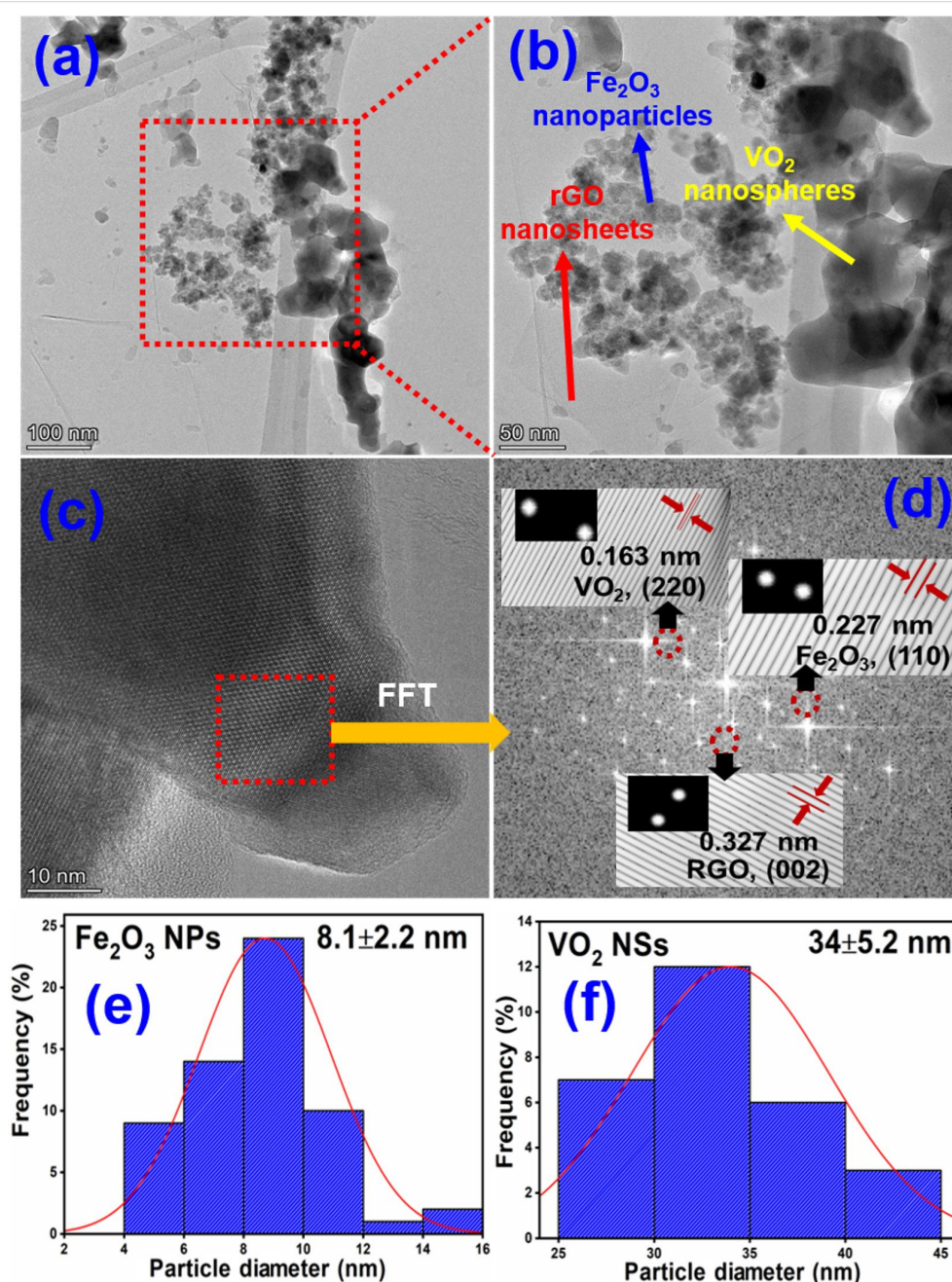


Figure 8: HRTEM analysis of GVF NC: (a, b) HRTEM images at low and high magnifications; (c, d) HRTEM images with corresponding FFT images; (e, f) average particle diameter of Fe_2O_3 NPs and VO_2 NSs.

ferent types of metal oxides on top of the rGO nanosheets (Figure 8e,f). Furthermore, the FFT analysis displays three planes with the d-spacing of 0.163, 0.227, and 0.327 nm, corresponding to the (220) plane of VO₂, (110) plane of Fe₂O₃, and (002) plane of rGO, respectively (Figure 8c,d). Overall, the detailed HRTEM analysis of GVF reveals the existence of two types of metal oxide on the rGO surface, which agrees with the previous SEM, XRD, and XPS analysis.

The magnetic properties of the GVF investigated at room temperature under an applied magnetic field ranging from –6000 Oe to 6000 Oe is shown in Figure 9. Herein, the saturation magnetization (M_s) value for GVF is reported to be 2.5 emu/g with a magnetic retentivity (M_{rs}) of 0.45 emu/g and coercivity of 141 Oe. Furthermore, it is speculated that the magnetic property in the case of GVF originates mostly from α -Fe₂O₃, with rGO being weakly magnetic and VO₂ being a non-magnetic material [42–45]. The presence of magnetic behavior in GVF further promotes the occurrence of iron oxide nanoparticles. Moreover, the low magnetic moment of GVF compared to that of native α -Fe₂O₃ nanoparticles (mostly synthesized through the Fe-based aqueous salt) could account for the low levels of α -Fe₂O₃ formed during the MW-assisted synthesis process while using ferrocene as the precursor. Additionally, it is to be noted that the formation of α -Fe₂O₃ nanoparticles in GVF originates from the Fe in the precursor (ferrocene). To further increase the magnetic behavior of GVF, the amount of precursor should be increased, which would result in a higher concentration of α -Fe₂O₃ nanoparticles. These composites could be applied in many areas of biomedicine, including contrast agents for MR imaging, cancer theragnostics, and tissue engineering.

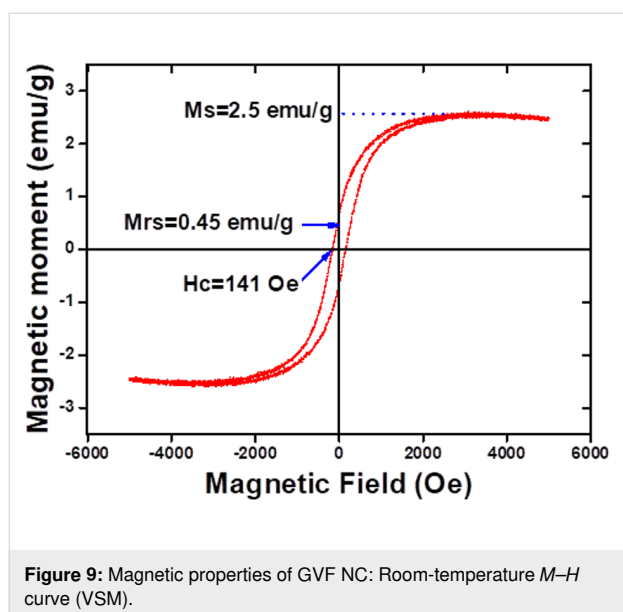


Figure 9: Magnetic properties of GVF NC: Room-temperature M – H curve (VSM).

Conclusion

In conclusion, a ternary NC consisting of α -Fe₂O₃, VO₂, and rGO was successfully synthesized through a simple, efficient, and low-cost MW approach. Compared to the reported synthetic approaches, the current technique is found to be beneficial in terms of time efficiency and cost-effectiveness. The synthesized NC was characterized through various techniques, including XRD, Raman, and XPS analyses. The morphological study revealed the deposition of α -Fe₂O₃ NPs and VO₂ nanorods on the rGO surface. Owing to the presence of magnetic components, the ternary NC displayed good magnetic characteristics at room temperature to showcase its potentiality in advanced biological applications. Further optimization of MW power and other reaction conditions can improve the characteristics of the composite, which could be the future prospects of the current work. Lastly, the current work opens a new door for synthesizing magnetic composites based on graphene materials along with metal oxides.

Funding

This work was supported by the 2024 Yeungnam University Research Grant.

Conflict of Interest

The authors declare that they have no known competing financial interests or personal relationships that could have appeared to influence the work reported in this paper.

Author Contributions

Sumanta Sahoo: conceptualization; data curation; formal analysis; methodology; writing – original draft. Ankur Sood: conceptualization; data curation; methodology; validation; writing – original draft. Sung Soo Han: funding acquisition; supervision; writing – review & editing.

ORCID® iDs

Sumanta Sahoo - <https://orcid.org/0000-0002-9429-3742>

Ankur Sood - <https://orcid.org/0000-0003-2328-0650>

Data Availability Statement

Data generated and analyzed during this study is available from the corresponding author upon reasonable request.

References

- Olabi, A. G.; Abdelkareem, M. A.; Wilberforce, T.; Sayed, E. T. *Renewable Sustainable Energy Rev.* **2021**, *135*, 110026. doi:10.1016/j.rser.2020.110026
- Lee, S. J.; Theerthagiri, J.; Nithyadharseni, P.; Arunachalam, P.; Balaji, D.; Madan Kumar, A.; Madhavan, J.; Mittal, V.; Choi, M. Y. *Renewable Sustainable Energy Rev.* **2021**, *143*, 110849. doi:10.1016/j.rser.2021.110849

3. Kumar, R.; Sahoo, S.; Pandey, R.; Joanni, E.; Yadav, R. M. *Mater. Sci. Eng., R* **2024**, *161*, 100860. doi:10.1016/j.mser.2024.100860
4. Kumar, R.; Sahoo, S.; Joanni, E.; Singh, R. K.; Yadav, R. M. *Mater. Today Nano* **2023**, *24*, 100399. doi:10.1016/j.mtnano.2023.100399
5. Carvalho, A. F.; Kulyk, B.; Fernandes, A. J. S.; Fortunato, E.; Costa, F. M. *Adv. Mater. (Weinheim, Ger.)* **2022**, *34*, 2101326. doi:10.1002/adma.202101326
6. Ghaffarkhah, A.; Hosseini, E.; Kamkar, M.; Sehat, A. A.; Dordanihaghghi, S.; Allahbakhsh, A.; van der Kuur, C.; Arjmand, M. *Small* **2022**, *18*, 2102683. doi:10.1002/sml.202102683
7. Nauman Javed, R. M.; Al-Othman, A.; Tawalbeh, M.; Olabi, A. G. *Renewable Sustainable Energy Rev.* **2022**, *168*, 112836. doi:10.1016/j.rser.2022.112836
8. Kumar, R.; Sahoo, S.; Joanni, E.; Singh, R. K. *J. Energy Chem.* **2022**, *74*, 252–282. doi:10.1016/j.jechem.2022.06.051
9. Kumar, R.; Sahoo, S.; Joanni, E.; Singh, R. K.; Kar, K. K. *ACS Appl. Mater. Interfaces* **2022**, *14*, 20306–20325. doi:10.1021/acsaami.1c15934
10. Kumar, R.; Sahoo, S.; Elfiky, M.; Pandey, R.; Yadav, R. M.; Tan, W. K.; Kawamura, G.; Matsuda, A.; Youssry, S. M. *Diamond Relat. Mater.* **2025**, *152*, 111924. doi:10.1016/j.diamond.2024.111924
11. Shahid, M.; Katugampalage, T. R.; Khalid, M.; Ahmed, W.; Kaewsaneha, C.; Sreearunothai, P.; Opaprakasit, P. *Sci. Rep.* **2022**, *12*, 19043. doi:10.1038/s41598-022-23622-x
12. Zhang, M.; Du, H.; Wei, Z.; Zhang, X.; Wang, R. *ACS Appl. Energy Mater.* **2021**, *4*, 8262–8274. doi:10.1021/acsaem.1c01507
13. Maity, C. K.; Sood, A.; Singhmar, R.; Choi, J. H.; Milton, A.; Choi, S. M.; Sahoo, S.; Han, S. S. *J. Alloys Compd.* **2025**, *1014*, 178734. doi:10.1016/j.jallcom.2025.178734
14. Kumar, R.; Singh, R. K.; Vaz, A. R.; Savu, R.; Moshkalev, S. A. *ACS Appl. Mater. Interfaces* **2017**, *9*, 8880–8890. doi:10.1021/acsaami.6b14704
15. Kumar, R.; Alaferdov, A. V.; Singh, R. K.; Singh, A. K.; Shah, J.; Kotnala, R. K.; Singh, K.; Suda, Y.; Moshkalev, S. A. *Composites, Part B* **2019**, *168*, 66–76. doi:10.1016/j.compositesb.2018.12.047
16. Staudenmaier, L. *Ber. Dtsch. Chem. Ges.* **1898**, *31*, 1481–1487. doi:10.1002/cber.18980310237
17. Xia, X.; Hao, Q.; Lei, W.; Wang, W.; Sun, D.; Wang, X. *J. Mater. Chem.* **2012**, *22*, 16844–16850. doi:10.1039/c2jm33064d
18. Xia, G.; Li, N.; Li, D.; Liu, R.; Wang, C.; Li, Q.; Lü, X.; Spendelow, J. S.; Zhang, J.; Wu, G. *ACS Appl. Mater. Interfaces* **2013**, *5*, 8607–8614. doi:10.1021/am402124r
19. Mummoorthi, G.; Shajahan, S.; Abu Haija, M.; Mahalingam, U.; Rajendran, R. *ACS Omega* **2022**, *7*, 27390–27399. doi:10.1021/acsomega.2c02418
20. Vignesh, S.; Suganthi, S.; Srinivasan, M.; Tamilmani, A.; Sundar, J. K.; Gedi, S.; Palanivel, B.; Shaikh, S. F.; Ubaidullah, M.; Raza, M. K. *J. Alloys Compd.* **2022**, *902*, 163705. doi:10.1016/j.jallcom.2022.163705
21. Kim, C.; Cho, K. M.; Park, K.; Kim, K. H.; Gereige, I.; Jung, H.-T. *ChemPlusChem* **2020**, *85*, 169–175. doi:10.1002/cplu.201900688
22. Ahmed, Z. N.; Ansari, M. Y.; Ansari, K. B.; Mesfer, M. K. A.; Danish, M.; Abushad, M.; Khan, W.; Raheman A. R., S. *ACS Appl. Electron. Mater.* **2024**, *6*, 3095–3109. doi:10.1021/acsaem.3c01217
23. Zhang, R.; Zhang, Z.; Qi, Y. *J. Alloys Compd.* **2025**, *1010*, 177753. doi:10.1016/j.jallcom.2024.177753
24. Athar, M. S.; Danish, M.; Muneer, M. *J. Environ. Chem. Eng.* **2021**, *9*, 105754. doi:10.1016/j.jece.2021.105754
25. Kumar, R.; Youssry, S. M.; Ya, K. Z.; Tan, W. K.; Kawamura, G.; Matsuda, A. *Diamond Relat. Mater.* **2020**, *101*, 107622. doi:10.1016/j.diamond.2019.107622
26. Guo, X.; Tan, Y.; Hu, Y.; Zafar, Z.; Liu, J.; Zou, J. *Sci. Rep.* **2021**, *11*, 21749. doi:10.1038/s41598-021-01025-8
27. Popuri, S. R.; Miclau, M.; Artemenko, A.; Labrugere, C.; Villesuzanne, A.; Pollet, M. *Inorg. Chem.* **2013**, *52*, 4780–4785. doi:10.1021/ic301201k
28. Zhang, C.; Wang, J.; Li, Y.; Li, X.; Koughia, C.; Wen, S.-J.; Wong, R.; Yang, Q.; Kasap, S. *Appl. Surf. Sci.* **2019**, *476*, 259–264. doi:10.1016/j.apsusc.2019.01.087
29. Kumar, R.; Singh, R. K.; Alaferdov, A. V.; Moshkalev, S. A. *Electrochim. Acta* **2018**, *281*, 78–87. doi:10.1016/j.electacta.2018.05.157
30. Hjiri, M. *J. Mater. Sci.: Mater. Electron.* **2020**, *31*, 5025–5031. doi:10.1007/s10854-020-03069-4
31. He, K.; Ma, F.-X.; Xu, C.-Y.; Cumings, J. *J. Appl. Phys.* **2013**, *113*, 17B528. doi:10.1063/1.4798500
32. Luo, Y. Y.; Su, F. H.; Pan, S. S.; Xu, S. C.; Zhang, C.; Pan, J.; Dai, J. M.; Li, P.; Li, G. H. *J. Alloys Compd.* **2016**, *655*, 442–447. doi:10.1016/j.jallcom.2015.08.254
33. Gupta, B.; Kumar, N.; Panda, K.; Kanan, V.; Joshi, S.; Visoly-Fisher, I. *Sci. Rep.* **2017**, *7*, 45030. doi:10.1038/srep45030
34. Chettri, P.; Vendamani, V. S.; Tripathi, A.; Pathak, A. P.; Tiwari, A. *Appl. Surf. Sci.* **2016**, *362*, 221–229. doi:10.1016/j.apsusc.2015.11.231
35. Soomro, S. A.; Gul, I. H.; Naseer, H.; Marwat, S.; Mujahid, M. *Curr. Nanosci.* **2019**, *15*, 420–429. doi:10.2174/1573413714666181115122016
36. Sahoo, S.; Al Mahmud, A.; Sood, A.; Dhakal, G.; Tiwari, S. K.; Zo, S.; Kim, H. M.; Han, S. S. *J. Sci.: Adv. Mater. Devices* **2025**, *10*, 100843. doi:10.1016/j.jsamd.2024.100843
37. Huelmo, C. P.; Menezes, M. G.; Capaz, R. B.; Denis, P. A. *Phys. Chem. Chem. Phys.* **2020**, *22*, 16096–16106. doi:10.1039/d0cp02167a
38. Bhatt, M. D.; Kim, H.; Kim, G. *RSC Adv.* **2022**, *12*, 21520–21547. doi:10.1039/d2ra01436j
39. Valencia, A. M.; Caldas, M. J. *Phys. Rev. B* **2017**, *96*, 125431. doi:10.1103/physrevb.96.125431
40. Martínez, J.; Dionizio, S.; Gutierrez, N.; Mosquera, E.; Diosa, J. E.; Bolaños, G.; Moran, O. *Appl. Phys. A: Mater. Sci. Process.* **2022**, *128*, 720. doi:10.1007/s00339-022-05798-1
41. Wang, X.; Mujtaba, J.; Fang, F.; Ahmad, M.; Arandiyani, H.; Yang, H.; Sun, G.; Sun, H. *RSC Adv.* **2015**, *5*, 91574–91580. doi:10.1039/c5ra16671c
42. Zysler, R. D.; Fiorani, D.; Testa, A. M. *J. Magn. Magn. Mater.* **2001**, *224*, 5–11. doi:10.1016/s0304-8853(00)01328-7
43. Raming, T. P.; Winnubst, A. J. A.; van Kats, C. M.; Philipse, A. P. *J. Colloid Interface Sci.* **2002**, *249*, 346–350. doi:10.1006/jcis.2001.8194
44. Sarkar, S. K.; Raul, K. K.; Pradhan, S. S.; Basu, S.; Nayak, A. *Phys. E (Amsterdam, Neth.)* **2014**, *64*, 78–82. doi:10.1016/j.physe.2014.07.014
45. McIntosh, R.; Mamo, M. A.; Jamieson, B.; Roy, S.; Bhattacharyya, S. *EPL* **2012**, *97*, 38001. doi:10.1209/0295-5075/97/38001

License and Terms

This is an open access article licensed under the terms of the Beilstein-Institut Open Access License Agreement (<https://www.beilstein-journals.org/bjnano/terms>), which is identical to the Creative Commons Attribution 4.0 International License (<https://creativecommons.org/licenses/by/4.0>). The reuse of material under this license requires that the author(s), source and license are credited. Third-party material in this article could be subject to other licenses (typically indicated in the credit line), and in this case, users are required to obtain permission from the license holder to reuse the material.

The definitive version of this article is the electronic one which can be found at:
<https://doi.org/10.3762/bjnano.16.70>



Synthesis of biowaste-derived carbon-dot-mediated silver nanoparticles and the evaluation of electrochemical properties for supercapacitor electrodes

Navya Kumari Tenkayala^{‡1,2}, Chandan Kumar Maity^{‡3}, Md Moniruzzaman^{*4} and Subramani Devaraju^{*1}

Full Research Paper

[Open Access](#)

Address:

¹Department of Chemistry, Vignan Foundation for Science, Technology and Research (Deemed to be University), Guntur, 522213, India, ²Department of Chemistry, Mallareddy college of Engineering and Technology, Maisammaguda, Dhulapally, Secundrabad, Telangana, 500100, India, ³Department of Chemistry, Gachon University, 1342 Seongnam-daero, Sujeong-gu, Seongnam-si, Gyeonggi-do 13120, Republic of Korea and ⁴Department of Chemical and Biological Engineering, Gachon University, 1342 Seongnam-daero, Seongnam-si, Gyeonggi-do 13120, Republic of Korea

Email:

Md Moniruzzaman^{*} - mani57chem@gachon.ac.kr;
Subramani Devaraju^{*} - subudeva@gmail.com

^{*} Corresponding author [‡] Equal contributors

Keywords:

asymmetric supercapacitor; carbon dots; fluorescence emission; green approach; silver nanoparticles

Beilstein J. Nanotechnol. **2025**, *16*, 933–943.
<https://doi.org/10.3762/bjnano.16.71>

Received: 14 February 2025

Accepted: 05 June 2025

Published: 24 June 2025

This article is part of the thematic issue "Fabrication, surface engineering and applications of new materials".

Guest Editor: S. K. Tiwari



© 2025 Tenkayala et al.; licensee Beilstein-Institut.
License and terms: see end of document.

Abstract

Herein, biowaste- (from *Pongamia pinnata* leaves) derived carbon dots (CDs) have been utilized as a mediator for the production of silver nanoparticles (PG-CDs-AgNPs) as a superior supercapacitor electrode. The methodology presented here is inexpensive and environmentally friendly as CDs play a role as capping, reducing, and stabilizing agent without addition of any chemicals. PG-CDs-AgNPs showed a particle size of 10 nm having excellent fluorescence emission in the blue region, and it has been explored as an electrode material for supercapacitor applications. The as-synthesized PG-CDs-AgNPs electrode exhibited the maximum specific capacitance of 540 F/g in a three-electrode study. The asymmetric supercapacitor (ASC) device with PG-CDs-AgNPs as the positive electrode reached the maximum specific capacitance of 200 F/g having a superior energy density of 71 W·h/kg at 1.5 A/g. Even at a high current density of 4 A/g, the ASC device reached a specific capacitance of 175 F/g, reinforcing its capability. The method described here provides a straightforward green approach towards biowaste-derived CD-mediated synthesis of AgNPs to produce efficient supercapacitor electrodes for energy storing.

Introduction

The extensive usage of fossil fuels is a result from the rising demand for energy. However, the use of fossil fuels is not sufficient to attend the energy demand. Therefore, a notable research focus has been given to advancements in renewable energy storage systems. Secondary batteries and supercapacitors are promising alternatives for energy storage applications [1,2]. Through the electrostatic polarization of electrolyte solutions, supercapacitor devices store charge across the electric double layers [3]. Supercapacitors are highly sought-after energy storage devices, as their high power density, ultrastability, and rapid charge–discharge capability render them irreplaceable by traditional metal-ion batteries [4]. Typically, the functioning of supercapacitors involves two different kinds of charge-storing mechanisms: pseudocapacitance and electric double-layer capacitance (EDLC) [5]. The reversible redox processes are the primary charge-storage mechanism for pseudocapacitors [6]. Even though the capacitance value of pseudocapacitors is theoretically very high, it is often followed by poor stability and an inferior specific energy density. This is due to the poor conducting nature, slow redox kinetics, as well as structural collapse which occurs throughout the redox progression [7]. EDLCs are able to provide desired stability, superior power density, quick charge/discharge capacity, and an outstanding retention rate. Nanocarbons are the appropriate candidates for EDLCs due to their high surface charge-storage ability and high conductivity [8–10]. The development of electrode materials with an efficient EDLC and pseudocapacitor properties is essential [11,12]. The cost-effective production of efficient electrode materials for supercapacitors is also very important. Researchers are exploring a wide range of new and affordable electrode materials, while maintaining the superior power and energy density. In this work, we have synthesized cost-effective carbon-dot- (CD) mediated silver nanoparticles (AgNPs) for supercapacitor electrodes.

AgNPs have garnered substantial interest due to their capacity to effectively facilitate biological, optical, chemical, electrical, and industrial applications [13,14]. AgNPs are widely utilized in electrochemical energy storage applications given their exceptional chemical durability, high electronic conductivity, and surface chemical characteristics. Due to these characteristics, AgNPs possess the capacity to function as the electrode material for supercapacitors. Numerous reports have also shown that AgNPs actively improve the electrochemical characteristics of different electrode materials. Salve et al. reported a noteworthy charge-storing capacity of 367.16 mF/cm² of the synthesized hybrid material, PGE/AgNPs/CS (pencil graphite electrodes/silver nanoparticles/chitosan) [15]. Lokhande et al. reached a specific capacitance (SC) of 424 F/g

for the Kimchi cabbage extract mediated AgNPs [16]. The enhanced performance was credited to the fact that the AgNPs were smaller, which meant that there was a bigger surface area for operative conducting pathways. Nevertheless, chemical reduction of Ag is extremely hazardous and can be dangerous to humans and the environment [17]. Hence, safer nontoxic methods for the production of AgNPs are in high demand.

Green chemistry emphasizes the use of nontoxic chemicals and production pathways for environmental safety. Motivated by these approaches, researchers have synthesized AgNPs utilizing green synthetic strategies which incorporate the utilization of plant extracts as reducing agents and stabilizing agents instead of traditional synthetic reducing agents such as NaBH₄ [16]. *Eclipta alba*, aloe vera, mint, and *Corchorous olitorious* are some of the plant extracts that have been selected as environmentally friendly reducing agents so far. However, the majority of these methods produce less stable and bigger particles, limiting their practical applicability and requiring more raw materials. CDs have a carbon core and surface functional groups which give them remarkable chemical and photophysical features, such as photostability, minimal toxicity, and tunable luminescence [18,19]. A significant number of studies has been carried out for developing CDs from inexpensive natural resources in many ways, which are also environment friendly. Instead of chemical precursors, plant materials such as mint, coriander, aloe, banana peel, and lemon were used to prepare carbon nanodots [20–24]. CDs have been recognized as green, effective agents for reducing metal ions to metal nanoparticles [25].

In this work, we focused on a green and facile synthetic way for the production of AgNPs utilizing CDs as reducing agent derived from *Pongamia pinnata* (*P. pinnata*) leaves. The novel aspect of this work is that a comprehensive green approach is verified throughout the process, starting with the choice of the CD precursor. The disadvantages of earlier research in this area include the need for a high reaction temperature and a drawn-out reaction process. However, this methodology does not involve any of these factors. The CDs have a dual behavior as it acts as a stabilizing and a reducing agent, resulting in the production of AgNPs with good water stability. The combination of EDLC-type CDs with pseudocapacitive AgNPs affords superior capacitive performance and stability, which are important for supercapacitor electrodes. The overall methodology along with the optical and electrochemical charge-storing performance have been schematically depicted in Supporting Information File 1, Scheme S1.

Experimental

Materials

All reagents of analytical grade were used for the experimental procedures. The details about all the chemicals are covered in Supporting Information File 1, section S1.

Synthesis of carbon dots from *Pongamia pinnata* leaves (PG-CDs)

For the synthesis of PG-CDs, 100 g of *Pongamia pinnata* leaves powder was taken into 1 L of water and stirred for 15 min at 60 °C on a magnetic stirrer. Procedures for the preparation of *Pongamia pinnata* leaves powder are discussed in Supporting Information File 1, section S1. Then, it was filtered by a Whatman filter paper and the extract was collected and placed on a magnetic stirrer with a sand bath maintained at 120 °C for 24 h. The color of the solution changed from orange to brown confirming the reaction progresses. After that, it was left alone until the reaction solution reached room temperature. Centrifugation was conducted for 5 min at 3000 rpm, followed by syringe filtration (0.22 µm) to discard larger agglomerated particles. Finally, the clear brown solution of PG-CDs was then kept in a refrigerator for additional experiments.

Synthesis of carbon-dot-mediated silver nanoparticles (PG-CDs-AgNPs)

The method for synthesizing AgNPs employing PG-CDs as both the reducing and stabilizing agents is as follows. PG-CDs-AgNPs were synthesized by adding the PG-CDs solution to 1 mM AgNO₃ in 1:10 V/V ratio in 100 mL of distilled water. The reaction was kept at room temperature undisturbed. The color changing from brown to dark brownish black confirmed the synthesis of PG-CDs-AgNP within 2 h. After 2 h of reaction, the sample was collected for UV–vis studies. The UV–vis spectra were also implemented at 12 and 24 h, respectively. The growth and the formation of PG-CDs-AgNP were recorded by using UV–vis spectroscopy.

Supporting Information File 1, section S1 contains the details of the material characterization techniques.

Results and Discussion

Plant extract-mediated production of nanoparticles from noble metal precursors are well reported. In the present work, waste *P. pinnata* leaf-derived CDs was utilized for the reduction of Ag⁺ to AgNPs. The efficient reduction of Ag(I) to Ag(0) at optimal concentrations of CDs confirmed the successful production of AgNPs from silver nitrate (AgNO₃). The adding of a small amount of PG-CDs to a 0.1 mM AgNO₃ solution (i.e., 1:9) produced AgNPs, as evidenced from the progressive color change of the solution as shown by surface plasmon resonance (SPR).

Structural and morphological analysis

The optical properties of PG-CDs and PG-CDs-AgNPs were studied using UV–visible spectroscopy and photoluminescence (PL) spectroscopy. An absorption peak at 275 nm was visualized in the UV–visible absorption spectrum of the PG-CDs, which is represented in Figure 1a. This peak might be accredited to the π – π^* transition of conjugated ($C_{sp^2}=C_{sp^2}$) aromatic domain of the PG-CDs [24]. Under the ultraviolet illuminator (365 nm), the brownish/red aqueous solution of the PG-CDs exhibited intense blue fluorescence (inset in Figure 1a), indicating the successful formation and photoluminescent nature of CDs. The formation of PG-CDs-AgNPs in the nanoscale is established by UV–visible spectroscopy by the appearance of SPR peaks at 475 nm [26]. The gradual emergence of absorption bands of PG-CDs-AgNPs was acquired at various time intervals to study the production and growth of nanoparticles over time. The gradual growth of PG-CDs-AgNPs has been checked and depicted in Figure 1b. The SPR peak was noticed within 2 h of reaction with PG-CDs, with a visible change in color of the solution to brownish black. The gradual increase in the peak intensity without any spectral shift of absorption maxima (λ_{max}) suggests that with increasing reaction time uniform-size stable nanoparticles were formed [27]. The excitation–wavelength-dependent emission spectra of the as-synthesized PG-CDs-AgNPs were recorded. As the excitation wavelength rises from 250 to 370 nm, the PL emission intensity gradually rises and the maximum PL emission intensity (430 nm) was attained at the excitation wavelength of 340 nm as displayed in Figure 1c. Figure 1d displays the excitation and emission contour map of PG-CDs-AgNPs, which suggests the PL emission in the blue range.

The crystalline nature of the PG-CDs-AgNPs was established from the X-ray diffraction pattern. Figure 2a displays an XRD pattern of the PG-CDs-AgNPs synthesized via PG-CDs mediated reduction. According to the XRD pattern, the phase composition could be classified according to the face-centered cubic structure of silver. The XRD spectrum showed that the formed PG-CDs-AgNPs were nanocrystals, as confirmed by the peaks at $2\theta \approx 28.20^\circ$, 32.66° , 38.61° , 46.60° , and 57.86° . These Bragg diffraction peaks are equivalent to the (110), (111), (121), (200), and (311) planes, which can be seen in the face-centered cubic structure of silver [28,29]. The XRD analysis of the PG-CDs-AgNPs produced via PG-CDs mediated reduction resembles the crystalline phase as referenced by (JCPDS File No. 84-0713) data [30].

Furthermore, the XPS analysis was implemented to study the elemental composition of PG-CDs-AgNPs and the corresponding chemical interaction between PG-CDs and AgNPs, as depicted in Figure 2b–d. As illustrated in Figure 2b, XPS total

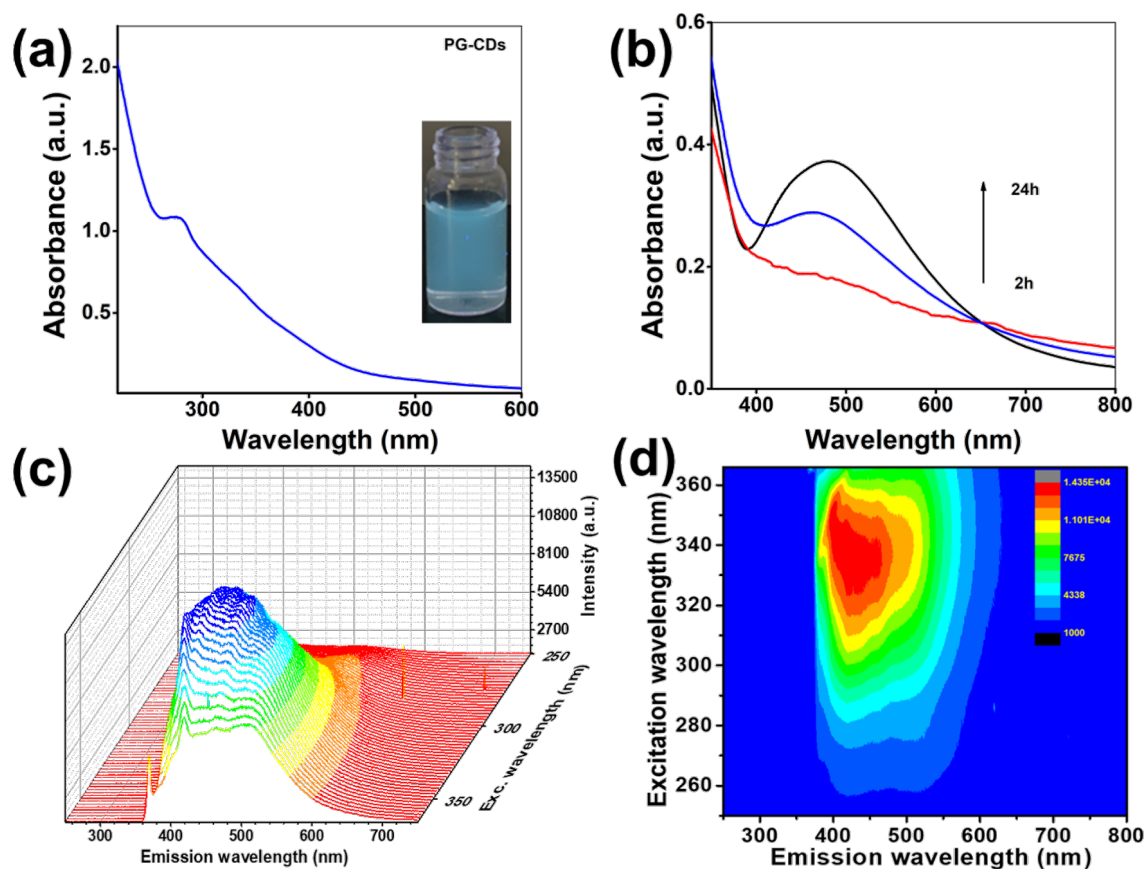


Figure 1: (a) UV–visible absorption spectrum of PG-CDs (the inset shows the digital photographic image of PG-CDs under the UV-illuminator). (b) UV–visible absorption spectra of PG-CDs-AgNPs at different time intervals. (c) Excitation–emission PL spectra of PG-CDs-AgNPs. (d) Excitation–emission contour map of PG-CDs-AgNPs.

survey profile of the PG-CDs-AgNPs is composed of carbon and silver elements, with binding energies of 285 and 368 eV, respectively. The high-resolution individual elemental XPS spectra of C 1s and Ag 3d are exhibited in Figure 2c–d. As shown in Figure 2d, the C 1s spectrum of the PG-CDs-AgNPs composite exhibited four primary peaks at binding energies of 282.9, 285.3, 287.1, and 288.5 eV. These peaks could be ascribed to the C–C (sp^3)/C=C (sp^2), C–O, C=O, and O–C=O groups, respectively [31]. In addition, the Ag 3d spectra (Figure 2c) of PG-CDs-AgNPs exhibited two characteristic peaks at binding energies of 368.7 and 374.6 eV equivalent to Ag 3d_{5/2} and Ag 3d_{3/2}, respectively [32]. It has been reported that the difference between the two peaks was around 6 eV, which indicates that silver was present in the PG-CDs-AgNPs in the form of nanoparticles of zero-valent silver [33]. Therefore, the XPS results proved that the PG-CDs-AgNPs were successfully synthesized. Additionally, CDs triggered the reduction of Ag⁺ to Ag(0) via oxygen-containing functionalities on their surfaces. The electrostatic attraction between the oxygen-containing functionalities on the surface of CDs binds with the positively charged Ag⁺ ions, which were then reduced by elec-

tron transfer from PG-CDs to the Ag⁺ ions [27]. The catechol moiety present in PG-CDs can form chelation with Ag⁺ ions. The Ag⁺ having a very high oxidation potential can easily be reduced to Ag(0) with concomitant oxidation of catechol to quinones. The quinones that are simultaneously created stabilize the AgNPs which are formed when the as-formed Ag(0) atoms in the reaction mixture collide with one another. This has been confirmed by the C 1s spectrum of CDs. The C–O group peak showed a decrease in intensity while the C=O group peak showed an increase in Figure 2d. This suggests that during the formation of the PG-CDs-AgNPs, the C–O groups on the surface of the CDs were oxidized and converted to C=O groups [34]. The mechanism for the production of PG-CDs-AgNPs has been illustrated in Figure 3.

The surface area of the supercapacitor electrode material is an important feature that can aid in surface charge storage. The specific surface area of the PG-CDs-AgNPs was determined using the Brunauer–Emmett–Teller (BET) analysis via the N₂ adsorption–desorption method, and equivalent BET isotherms are depicted in Supporting Information File 1, Figure S1a. The

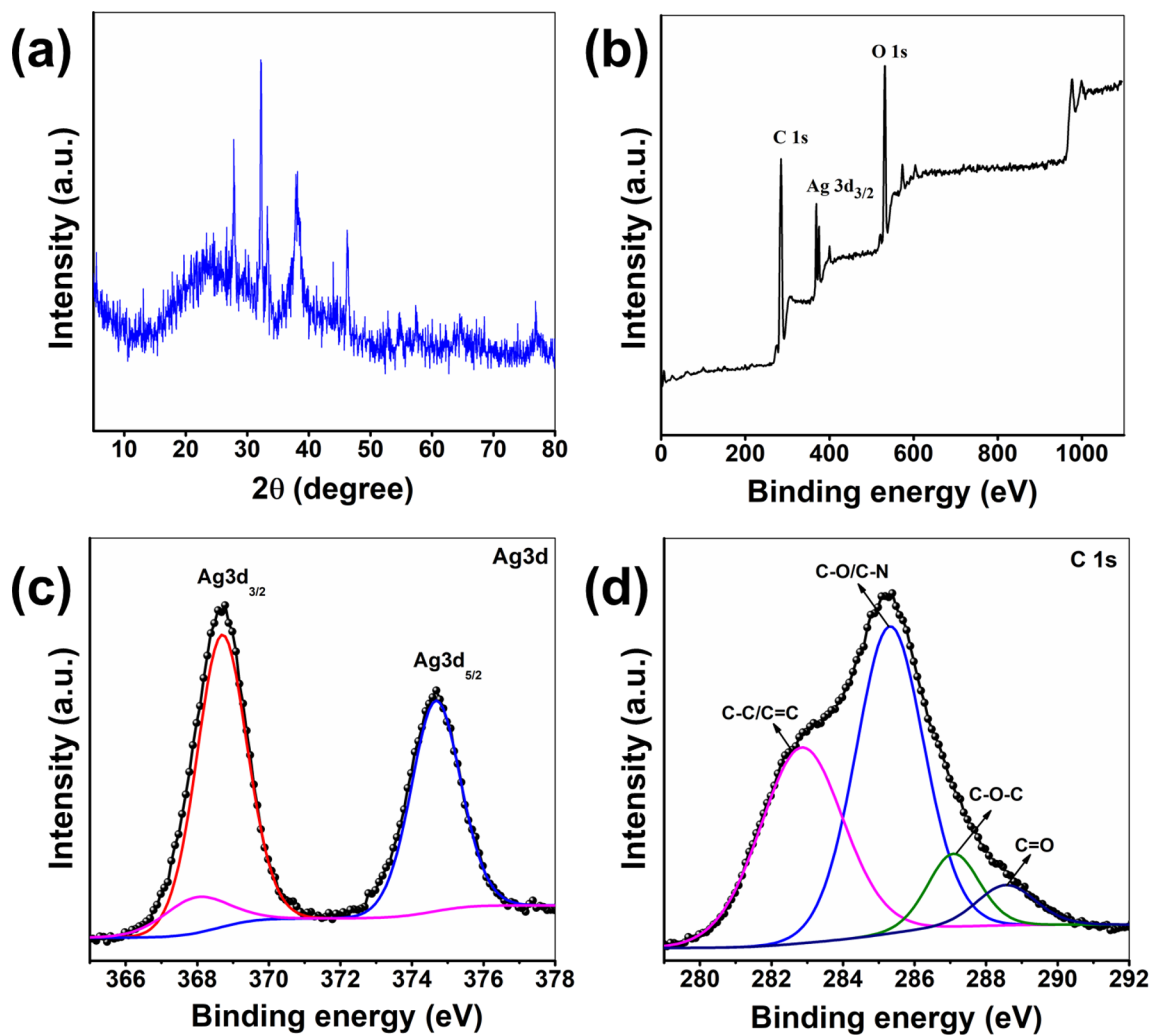


Figure 2: (a) XRD patterns of PG-CDs-AgNPs; XPS analysis of PG-CDs-AgNPs: (b) XPS survey profile; deconvoluted XPS spectra of (c) Ag 3d and (d) C 1s.

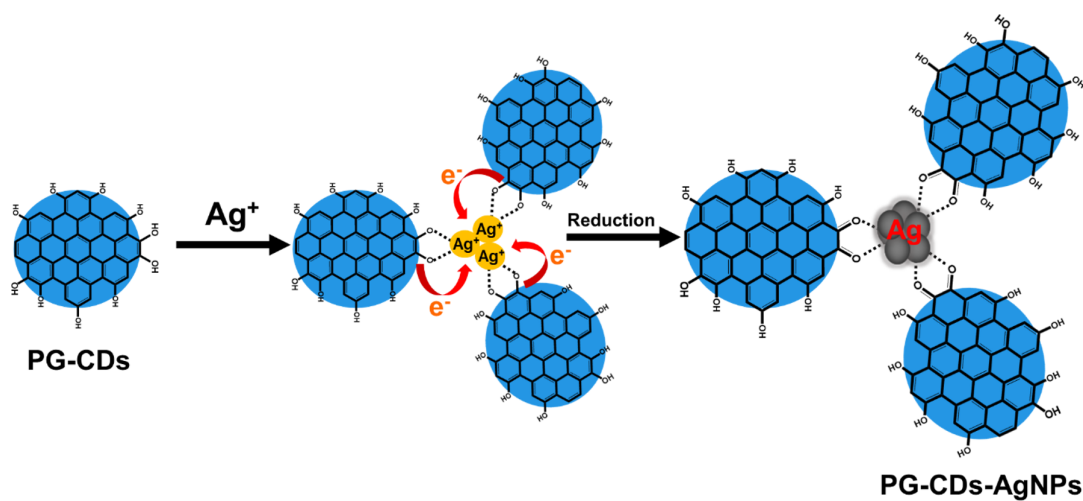


Figure 3: Formation and stabilization of PG-CDs-AgNPs.

surface area of PG-CDs-AgNPs was found to be 83.04 m²/g. A uniform nanoscale particle distribution of PG-CDs-AgNPs was responsible for the enhanced surface area [35]. The pore size distribution plot of PG-CDs-AgNPs suggests the mesoporous characteristics (Supporting Information File 1, Figure S1b), which, via the diffusion of electrolyte ions, is highly efficient for electrochemical charge storage.

The size distribution, morphology, and crystallinity of PG-CDs-AgNPs were further characterized by SEM and TEM analysis. The SEM image of PG-CDs-AgNPs (Supporting Information File 1, Figure S2a) reveals that PG-CDs-AgNPs possess spherical and distorted spherical structure. Supporting Information File 1, Figure S2b depicts the EDX mapping of PG-CDs-AgNPs, which proves the existence of Ag, C, and O in PG-CDs-AgNPs, and the atomic weight percentage (%) of the corresponding elements are given in the inset table (Supporting Information File 1, Figure S2b). The elemental mapping analysis for the PG-CDs-AgNPs proves the existence of O, C, and Ag (Supporting Information File 1, Figure S2c–e). Figure 4a–c displays TEM images of PG-CDs-AgNPs with different scale bars exhibiting that the particles are spherical and uniformly distributed. Figure 4d is the HR-TEM image of PG-CDs-

AgNPs, exhibiting a well-resolved lattice spacing of 0.24 nm equivalent to (111) lattice planes of silver [36]. The clear visible lattice fringe indicates that the particles are crystalline. The average particle size distribution histogram depicted that the diameter of PG-CDs-AgNPs were approximately 9–10 nm, as depicted in Figure 4e. The narrowness of the average particle size distribution plot was well supported by the uniform particle size distribution shown in TEM images. Figure 4f is the selected area electron diffraction (SAED) pattern of PG-CDs-AgNPs, exhibiting a ring-like diffraction pattern indicating crystalline nature. The ring-like diffraction suggests the (111) plane. The symmetry in the diffraction spots indicates that the spherical particles possess a high degree of crystallinity. Thus, both the SAED pattern and HRTEM image suggest that the synthesized spherical PG-CDs-AgNPs are nanocrystals.

Electrochemical properties of the synthesized electrode

Three-electrode analysis

Firstly, utilizing a three-electrode configuration in an aqueous electrolyte (1 M aqueous KCl), the electrochemical properties (capacitive characteristics, charge transportation, and charging/discharging) of PG-CDs-AgNPs were examined within a

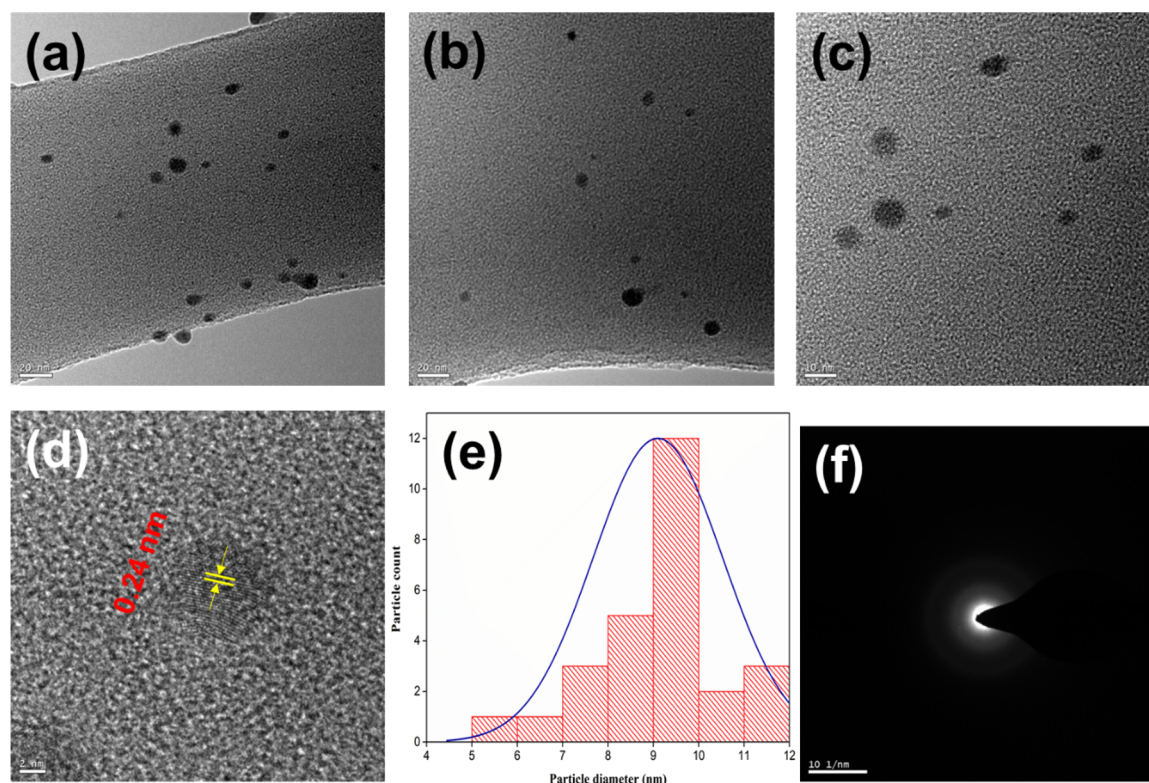


Figure 4: TEM images (a–c) of PG-CDs-AgNPs; (d) HRTEM image of PG-CDs-AgNPs, (e) average particle size distribution histogram, and (f) SAED patterns PG-CDs-AgNPs.

0–0.8 V potential window. Aqueous (aq.) electrolytes are inexpensive, readily accessible, and environmentally benign. In this case, KCl (aq.) is neutral and contains small-sized, highly mobile K^+ and Cl^- ions. These ions should be easier to reach in order to optimize the electrochemical activity, which can then optimize the capacitive response. Supporting Information File 1, section S1 contains the details of the electrochemical characterization techniques.

Figure 5a depicts the CV plot of PG-CDs-AgNPs electrode at various scan rates (5–200 mV/s). It is evident through the PG-CDs-AgNPs CV graph that as the scan rates are increased, the current densities rise owing to the quicker diffusion kinetics on the electrode surface [37]. A lower scan rate means that the entire voltammogram takes longer to complete than a high scan rate. At low scan rates, diffusion layers extend further from the electrode surface, resulting in reduced electrode flux compared to that of higher scan rates. This occurs because current densities are influenced by the rate of scanning [37]. The higher cur-

rent density at 200 mV/s suggests that, at this specific scan rate, the ion transport rate and the reactions for the interfacial charge storing are possible. The good capacitive characteristics and faster reversible electrochemical reactions of the electrode are also indicated by the comparable cyclic voltammogram at high scan speeds. Electric double-layer capacitance, not pseudocapacitance, is the main charge-storage mechanism for PG-CDs-AgNPs, as evidenced by the quasi-rectangular CV profile [38]. The electrochemistry of any electrode material is purposefully controlled by the composition of the electrolyte. Since KCl is used as a neutral electrolyte, PG-CDs-AgNPs exhibit capacitive behavior through a surface-charge-storing EDLC-type mechanism. Given the low charge density of K^+ ions, which facilitates its access to the electrode during the electrochemical reaction, it may be concluded that this occurrence may have an impact on the performance of the electrochemical reaction. The deintercalation and intercalation of electrolyte ions on the surface of electrode, the efficient dispersion of electrolyte ions within the pores of PG-CDs-AgNPs and on their surface, and

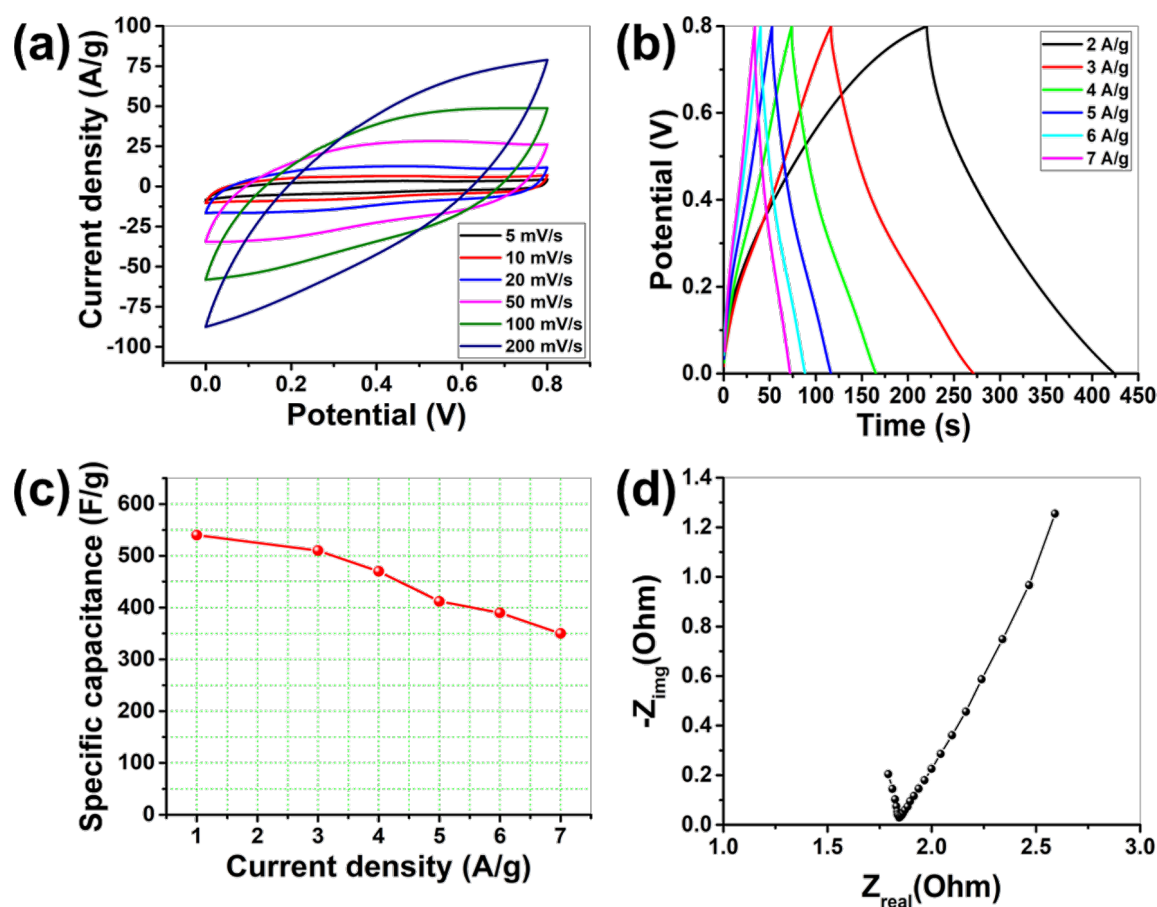


Figure 5: Electrochemical analysis of PG-CDs-AgNPs in 1 M aq. KCl using a three-electrode set-up: (a) CV plots of PG-CDs-AgNPs at various scan rates (5–200 mV/s), (b) GCD analysis of PG-CDs-AgNPs at various current densities, (c) SC as a function of current density of CDs-AgNPs electrode at various current densities, and (d) Nyquist graph of PG-CDs-AgNPs electrode.

the high mobility of cations and anions within the electrolyte are the three mechanisms that allow PG-CDs-AgNPs to store charge during electrochemical reactions.

In order to ascertain the SC of PG-CDs-AgNPs, the galvanostatic charge/discharge (GCD) experiment was further implemented within the potential window of 0–0.8 V using the similar electrolyte and electrode configurations as the CV test (Figure 5b). The symmetric GCD profiles of PG-CDs-AgNPs demonstrate the neutral reversibility of the electrolyte and predominant EDLC behavior during the charge–discharge progression. Additionally, the GCD analysis showed that PG-CDs-AgNPs had 100% coulombic efficiency. Supporting Information File 1, Equation S1 was considered to measure the SC from the discharge time obtained from the GCD measurement. Higher SCs are demonstrated by electrode materials with longer discharge durations. At 2 A/g, the obtained SC for PG-CDs-AgNPs was found to be 540 F/g. Figure 5c exemplifies plots of the current density as a function of SC of PG-CDs-AgNPs at multiple current densities. Due to its superior rate capability at a high current density of 7 A/g, this electrode even had a decent SC of 350 F/g. Only around 35% of the initial SC is lost by the PG-CDs-AgNPs at a high current density. With respect to time, the electrolyte ions stimulated the electrode material, which was responsible for the decent rate capability and superior capacity of the PG-CDs-AgNPs electrode.

To evaluate the capability of charge carrying within the electrode and the capacitive property of PG-CDs-AgNPs, electrochemical impedance spectroscopy (EIS) measurements were also implemented. The Nyquist plots of the PG-CDs-AgNPs are displayed in Figure 5d. The charge-transfer resistance (R_{ct}) in the high-frequency range is indicated by the semicircle diameter [39,40]. How facile electrons or ions can be moved throughout the electrode and electrolyte–electrode system is shown by the R_{ct} [39,40]. The straight line in the low-frequency range of the EIS graphic describes the capacitive properties [37]. The equivalent series resistance (R_{ESR}), which is often generated from the ohmic and interfacial resistance of the electrolyte and electrode, respectively, is designated by the intersection of the semicircle on the real axis [37,41]. The minimal interfacial resistance is confirmed by the PG-CDs-AgNPs reduced R_{ESR} value. Easy electrolyte ion transport through highly conducting CDs is the primary cause of the decreased R_{ESR} and R_{ct} for PG-CDs-AgNPs. Above all, the fact that the straight line in the case of PG-CDs-AgNPs has a greater slope suggests that these particles have optimal supercapacitive properties and electrochemical activity. In the three-electrode investigation, PG-CDs-AgNPs showed better electrochemical activity overall in terms of capacitive performance, charge-transfer activity, and discharge time.

Electrochemical analysis of the asymmetric supercapacitor device in a 1 M TEABF₄/DMSO organic electrolyte

Electrochemical evaluations attributed that in the three-electrode configuration, the PG-CDs-AgNPs electrode possessed superior electrochemical activity. Thus, utilizing carbon black (CB) as the negative electrode and PG-CDs-AgNPs as the positive electrode, an ASC device was built for real-time application. Supporting Information File 1, section S2 covers the device assembly processes. A figure of the ASC device is portrayed in Figure 6a. All electrochemical activities of the supercapacitor device were evaluated using 1 M TEABF₄/DMSO, an organic electrolyte. The consistent operating potential window of the electrolyte is crucial for an electrochemical device. The overpotential of water limits the stable functioning voltages of aqueous electrolytes to about 1.0 V, despite the fact that they are readily available, easy to handle, and environmentally friendly. Organic electrolytes, on the other hand, provide larger potential windows for electrochemical devices. The organic electrolyte 1 M TEABF₄/DMSO can provide a stable working potential window. Due to its strong polarity and decent ionic mobility, TEABF₄/DMSO may be helpful in maximizing the electrochemical activity.

Comprehensive electrochemical experiments, such as cyclic stability, EIS, GCD, and CV evaluations, were conducted on the ASC device. A CV test (Figure 6b) of the ASC device was first performed at a fixed scan rate of 50 mV/s with changing the voltage windows (up to 1.8 V). This showed that the features of the CV curve did not expressively deviate in the organic electrolyte when the potential limits were varied from 1.0 to 1.8 V. The CV experiment shows that the ASC was functioning within the range of 0 to 1.8 V, which is the maximum stable operating potential. The CV profiles of the device are shown in Figure 6c at various scan rates (20–500 mV/s) within the 0–1.8 V maximum voltage limit. The areas and current responses of the cyclic voltammograms rose with an increasing scan rate, similar to the three-electrode investigation, due to the faster diffusion kinetics on the surface of the electrode. At high scan rates (such as 500 mV/s), there was no discernible diversion of the features of the CV profiles. The current responsiveness of the device was adequate even at a 20 mV/s scan rate. For real-time applications, the capacitive effectiveness of PG-CDs-AgNPs as an ASC electrode shows enormous promise. The largest pseudocapacitance contribution of the PG-CDs-AgNPs electrode was indicated by the CV graphs, which considerably diverged from their true rectangular shape. In order to determine the SC of the device, a GCD analysis was also carried out at various potential limitations (1.0–1.6 V); Figure 6d shows the GCD plots. The operating voltage limit was accompanied by an improvement in both the energy density (ED) and SC. Addition-

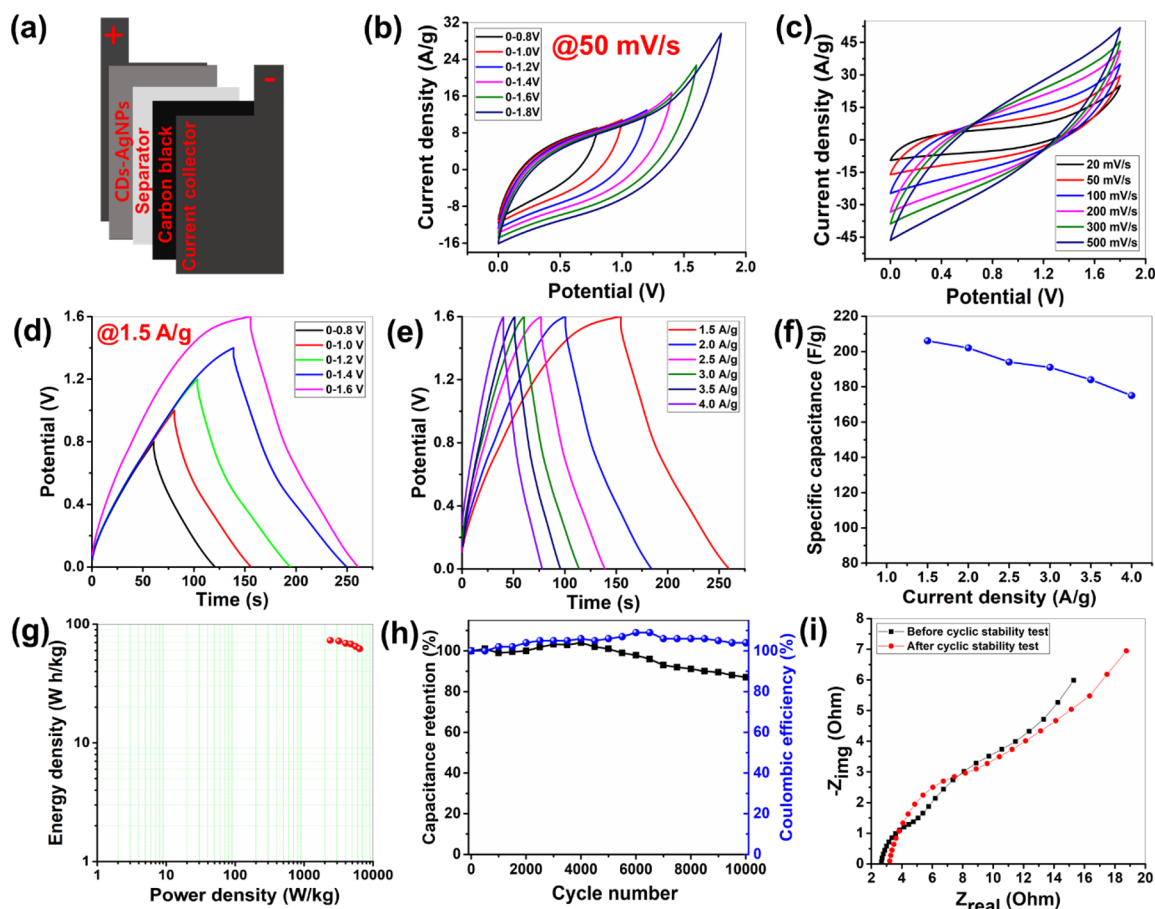


Figure 6: (a) Schematic image of the ASC device using PG-CDs-AgNPs and CB as positive and negative electrodes, respectively. In the organic electrolyte, the electrochemical evaluations of the ASC device are: (b) CV analysis in different voltage limits at 50 mV/s, (c) CV analysis at different scan rates (20–500 mV/s) within 0–1.8 V, (d) GCD plots in various potential limits at 1.5 A/g, (e) GCD profiles at various current densities (1.5–4 A/g) within 0–1.6 V, (f) SC as a function of current density graph of the ASC device, (g) Ragone plot, (h) cyclic stability and coulombic efficiency plot, and (i) before and after cyclic stability Nyquist plots.

ally, when the current density increased, the GCD plot features did not change (Figure 6e). Figure 6f demonstrates the current density as a function of SC of the ASC device at multiple current densities. The ASC reached the maximum SC of 200 F/g, while the maximum ED was 71 W·h/kg at 1.5 A/g in the organic electrolyte. The SC of 175 F/g was demonstrated by the ASC device even at a high current density of 4 A/g, confirming the required rate capacity of the PG-CDs-AgNPs-based ASC. Only around 12.5% of the initial SC was lost by the PG-CDs-AgNPs at a high current density. A suitable rate capability and decent electrochemical activities are ascribed to the contribution from pseudocapacitance and EDLC and the synergistic involvement of CDs and Ag NPs. The small IR drop seen by the ASC device indicates that all of the electrode capacitance is present within the operational voltage. Figure 6g illustrates the Ragone plot of the device which achieved the maximum ED of 71 W·h/kg. The ASC device also showed the highest power

density (PD) of 6400 W/kg, while sustaining 62 W·h/kg ED. The stability of this ASC device over 10,000 GCD cycles was also assessed. After the accomplishment of 10,000 GCD cycles, the ASC showed ≈87% SC retention (Figure 6h). The capacitance retention of the device improved over the first 4000 cycles as the electrolyte ions gradually permeated the electrode pores, activating both the anode and cathode materials. A slight decline in the capacitance retention was primarily attributed to the progressive mechanical deformation of the electrode material and the partial detachment of active materials from the current collectors. The cyclic stability of the PG-CDs-AgNPs nanohybrid as the positive electrode for ASC has also been compared with similar types of electrodes, as summarized in Supporting Information File 1, Table S1. The Coulombic efficiency of the device was also measured up to 10000 cycles and the device exhibited almost 100% of coulombic efficiency. Following the cyclic stability test, the EIS analysis was also

performed. The Nyquist plots of the device before and after stability tests are presented in Figure 6i. Before the cyclic stability test, the R_{ESR} value of this ASC was found to be 2.6 Ω . However, the R_{ESR} value was increased to 3.2 Ω after the stability test, and this is mostly owing to the deformation and degradation of the electrode material during the electrochemical progression.

Conclusion

A green synthetic method was successfully adopted for the production of AgNPs using CDs produced from waste biomass as a stabilizing and reducing agent. The TEM analysis showed that the produced PG-CDs-AgNPs have more uniform surfaces and spherical shapes with an average particle size of 10–11 nm. The synthesized PG-CD-AgNPs are crystalline with CDs support, confirmed by SEAD patterns and XRD. The synthesized PG-CDs-AgNPs electrode showed a maximum SC value of 540 F/g at 1 A/g in the three-electrode system. Besides, the ASC device constructed with PG-CDs-AgNPs reached a decent energy density of 71 W·h/kg with $\approx 87\%$ retention of SC after 10,000 GCD cycles. Decent electrochemical properties of PG-CDs-AgNPs confirm that PG-CDs-AgNPs could be a promising contender for energy storage devices.

Supporting Information

Supporting Information File 1

Experimental procedures including materials details and characterizations; Schematic representation; BET isotherm and pore size distribution plot; SEM, EDX, and elemental mapping of PG-CDs-AgNPs; ASC device fabrication method; Table for the comparison of cyclic stability. [<https://www.beilstein-journals.org/bjnano/content/supplementary/2190-4286-16-71-S1.pdf>]

Acknowledgements

GITAM, Hyderabad is appreciated by N.K.T for providing laboratory facilities.

Conflict of Interest

Nothing to declare.

Author Contributions

Navya Kumari Tenkayala: conceptualization; data curation; formal analysis; methodology; visualization; writing – original draft. Chandan Kumar Maity: conceptualization; data curation; formal analysis; investigation; methodology; validation; visualization; writing – original draft. Md Moniruzzaman: conceptualization; data curation; formal analysis; investigation; methodol-

ogy; supervision; validation; writing – review & editing. Subramani Devaraju: conceptualization; funding acquisition; investigation; project administration; resources; supervision; validation; writing – review & editing.

ORCID® iDs

Md Moniruzzaman - <https://orcid.org/0000-0002-8900-2752>

Subramani Devaraju - <https://orcid.org/0000-0003-1859-1163>

Data Availability Statement

Data generated and analyzed during this study is available from the corresponding author upon reasonable request.

References

- Waris; Chaudhary, M. S.; Anwer, A. H.; Sultana, S.; Ingole, P. P.; Nami, S. A. A.; Khan, M. Z. *Energy Fuels* **2023**, *37*, 19433–19460. doi:10.1021/acs.energyfuels.3c03213
- Dhandapani, E.; Duraisamy, N.; Rajedran, R. *ACS Appl. Polym. Mater.* **2023**, *5*, 7420–7432. doi:10.1021/acsapm.3c01237
- Simon, P.; Gogotsi, Y. *Nat. Mater.* **2008**, *7*, 845–854. doi:10.1038/nmat2297
- Maity, C. K.; De, S.; Acharya, S.; Siddiki, S. H.; Sahoo, S.; Verma, K.; Thakur, V. K.; Nayak, G. C. *J. Energy Storage* **2022**, *56*, 105928. doi:10.1016/j.est.2022.105928
- Atika; Dutta, R. K. *Energy Fuels* **2023**, *37*, 8637–8649. doi:10.1021/acs.energyfuels.3c00600
- Luo, W.; Quan, H.; Zhang, Z.; Wang, Y.; Xie, X.; Hong, Z.; Chen, D. *ACS Appl. Nano Mater.* **2021**, *4*, 12051–12061. doi:10.1021/acsanm.1c02606
- Thomas, B.; George, G.; Landström, A.; Concina, I.; Geng, S.; Vomiero, A.; Sain, M.; Oksman, K. *ACS Appl. Electron. Mater.* **2021**, *3*, 4699–4710. doi:10.1021/acsaem.1c00487
- Bhowmik, T.; Mishra, R.; Barman, S. *Energy Fuels* **2021**, *35*, 5206–5216. doi:10.1021/acs.energyfuels.0c03613
- Hou, X.; Zhang, Q.; Wang, L.; Gao, G.; Lü, W. *ACS Appl. Mater. Interfaces* **2021**, *13*, 12432–12441. doi:10.1021/acsami.0c18741
- Li, L.; Li, Y.; Ye, Y.; Guo, R.; Wang, A.; Zou, G.; Hou, H.; Ji, X. *ACS Nano* **2021**, *15*, 6872–6885. doi:10.1021/acsnano.0c10624
- De, S.; Maity, C. K.; Kim, M. J.; Nayak, G. C. *Electrochim. Acta* **2023**, *463*, 142811. doi:10.1016/j.electacta.2023.142811
- Maity, C. K.; De, S.; Panigrahi, A.; Acharya, S.; Verma, K.; Kim, M. J.; Nayak, G. C. *Composites, Part B* **2023**, *264*, 110887. doi:10.1016/j.compositesb.2023.110887
- Khodadadi, B.; Bordbar, M.; Yeganeh-Faal, A.; Nasrollahzadeh, M. *J. Alloys Compd.* **2017**, *719*, 82–88. doi:10.1016/j.jallcom.2017.05.135
- Pahlavan Noghabi, M.; Parizadeh, M. R.; Ghayour-Mobarhan, M.; Taherzadeh, D.; Hosseini, H. A.; Darroudi, M. *J. Mol. Struct.* **2017**, *1146*, 499–503. doi:10.1016/j.molstruc.2017.05.145
- Salve, M.; Mandal, A.; Amreen, K.; Pattnaik, P. K.; Goel, S. *Microchem. J.* **2020**, *157*, 104973. doi:10.1016/j.microc.2020.104973
- Lokhande, A. C.; Babar, P. T.; Karade, V. C.; Jang, J. S.; Lokhande, V. C.; Lee, D. J.; Kim, I.-C.; Patole, S. P.; Qattan, I. A.; Lokhande, C. D.; Kim, J. H. *Mater. Today Chem.* **2019**, *14*, 100181. doi:10.1016/j.mtchem.2019.07.003
- Arnou, P.; Cooper, C. S.; Malkov, A. V.; Bowers, J. W.; Walls, J. M. *Thin Solid Films* **2015**, *582*, 31–34. doi:10.1016/j.tsf.2014.10.080

18. Kooshki, H.; Sobhani-Nasab, A.; Eghbali-Arani, M.; Ahmadi, F.; Ameri, V.; Rahimi-Nasrabadi, M. *Sep. Purif. Technol.* **2019**, *211*, 873–881. doi:10.1016/j.seppur.2018.10.057
19. Sobhani-Nasab, A.; Hoseinpour, S. M.; Rahimi-Nasrabadi, M.; Pourmasoud, S.; Eghbali-Arani, M.; Ahmadi, F. *J. Mater. Sci.: Mater. Electron.* **2021**, *32*, 26998–27013. doi:10.1007/s10854-021-07073-0
20. Sachdev, A.; Gopinath, P. *Analyst* **2015**, *140*, 4260–4269. doi:10.1039/c5an00454c
21. Raveendran, V.; Suresh Babu, A. R.; Renuka, N. K. *RSC Adv.* **2019**, *9*, 12070–12077. doi:10.1039/c9ra02120e
22. Xu, H.; Yang, X.; Li, G.; Zhao, C.; Liao, X. *J. Agric. Food Chem.* **2015**, *63*, 6707–6714. doi:10.1021/acs.jafc.5b02319
23. Atchudan, R.; Jebakumar Immanuel Edison, T. N.; Shanmugam, M.; Perumal, S.; Somanathan, T.; Lee, Y. R. *Phys. E (Amsterdam, Neth.)* **2021**, *126*, 114417. doi:10.1016/j.physe.2020.114417
24. Ding, H.; Zhou, X.; Qin, B.; Zhou, Z.; Zhao, Y. *J. Lumin.* **2019**, *211*, 298–304. doi:10.1016/j.jlumin.2019.03.064
25. Lu, Q.; Deng, J.; Hou, Y.; Wang, H.; Li, H.; Zhang, Y.; Yao, S. *Chem. Commun.* **2015**, *51*, 7164–7167. doi:10.1039/c5cc01771h
26. Yallappa, S.; Manjanna, J.; Dhananjaya, B. L. *Spectrochim. Acta, Part A* **2015**, *137*, 236–243. doi:10.1016/j.saa.2014.08.030
27. Varsha Raveendran, P. T.; Renuka, N. K. *Environ. Nanotechnol. Monit. Manage.* **2022**, *18*, 100676. doi:10.1016/j.enmm.2022.100676
28. Namburi, K. R.; Kora, A. J.; Chetukuri, A.; Kota, V. S. M. K. *Bioprocess Biosyst. Eng.* **2021**, *44*, 1975–1988. doi:10.1007/s00449-021-02579-7
29. Tenkayala, N. K.; Katari, N. K.; Gundla, R.; Jonnalagadda, S. B.; Devaraju, S. *Mater. Res. Express* **2024**, *11*, 015005. doi:10.1088/2053-1591/ad1128
30. Sagadevan, S.; Vennila, S.; Singh, P.; Lett, J. A.; Johan, M. R.; Marlinda, A. R.; Muthiah, B.; Lakshmipathy, M. *Green Process. Synth.* **2019**, *8*, 873–884. doi:10.1515/gps-2019-0058
31. Ramaraghavulu, R.; Rao, V. K.; Devarayapalli, K. C.; Yoo, K.; Nagajyothi, P. C.; Shim, J. *Res. Chem. Intermed.* **2021**, *47*, 637–648. doi:10.1007/s11164-020-04290-w
32. Mohamedkhair, A. K.; Drmosh, Q. A.; Yamani, Z. H. *Front. Mater.* **2019**, *6*, 188. doi:10.3389/fmats.2019.00188
33. Ghodake, G.; Shinde, S.; Saratale, R. G.; Kadam, A.; Saratale, G. D.; Patel, R.; Kumar, A.; Kumar, S.; Kim, D.-Y. *Microchim. Acta* **2019**, *186*, 763. doi:10.1007/s00604-019-3877-8
34. Quites, F. J.; Azevedo, C. K. S.; Alves, E. P. P.; Germino, J. C.; Vinhas, R. C. G.; Landers, R.; Terezo, A. J.; Atvars, T. D. Z. *J. Braz. Chem. Soc.* **2017**, *28*, 106–115. doi:10.5935/0103-5053.20160152
35. Zhang, S.; Sui, L.; Dong, H.; He, W.; Dong, L.; Yu, L. *ACS Appl. Mater. Interfaces* **2018**, *10*, 12983–12991. doi:10.1021/acsami.8b00323
36. Momin, B.; Rahman, S.; Jha, N.; Annapure, U. S. *Bioprocess Biosyst. Eng.* **2019**, *42*, 541–553. doi:10.1007/s00449-018-2057-2
37. Maity, C. K.; Sahoo, S.; Verma, K.; Behera, A. K.; Nayak, G. C. *New J. Chem.* **2020**, *44*, 8106–8119. doi:10.1039/c9nj06284j
38. Wang, R.; Li, X.; Nie, Z.; Zhao, Y.; Wang, H. *J. Energy Storage* **2021**, *38*, 102479. doi:10.1016/j.est.2021.102479
39. Zhang, X.; Ge, X.; Sun, S.; Qu, Y.; Chi, W.; Chen, C.; Lü, W. *CrystEngComm* **2016**, *18*, 1090–1095. doi:10.1039/c5ce02038g

40. Xiong, P.; Zhu, J.; Wang, X. *Ind. Eng. Chem. Res.* **2013**, *52*, 17126–17133. doi:10.1021/ie402437k

41. Maity, C. K.; Sahoo, S.; Verma, K.; Nayak, G. C. *Energy Fuels* **2022**, *36*, 2248–2259. doi:10.1021/acs.energyfuels.1c04436

License and Terms

This is an open access article licensed under the terms of the Beilstein-Institut Open Access License Agreement (<https://www.beilstein-journals.org/bjnano/terms>), which is identical to the Creative Commons Attribution 4.0 International License (<https://creativecommons.org/licenses/by/4.0>). The reuse of material under this license requires that the author(s), source and license are credited. Third-party material in this article could be subject to other licenses (typically indicated in the credit line), and in this case, users are required to obtain permission from the license holder to reuse the material.

The definitive version of this article is the electronic one which can be found at:

<https://doi.org/10.3762/bjnano.16.71>



Single-layer graphene oxide film grown on α -Al₂O₃(0001) for use as an adsorbent

Shiro Entani^{*1}, Mitsunori Honda², Masaru Takizawa³ and Makoto Kohda^{1,4}

Full Research Paper

Open Access

Address:

¹Quantum Materials and Applications Research Center, National Institutes for Quantum Science and Technology, Takasaki, Gunma 370-1292, Japan, ²Honda's Lab for Development of Future Clay Materials Research, Japan Atomic Energy Agency, Tokai, Ibaraki 319-1195, Japan, ³College of Science and Engineering, Ritsumeikan University, Kusatsu, Shiga 525-8577, Japan and ⁴School of Engineering, Tohoku University, Aoba-ku, Sendai 980-8579, Japan

Email:

Shiro Entani^{*} - entani.shiro@qst.go.jp

^{*} Corresponding author

Keywords:

cesium adsorption; chemical vapor deposition; electronic state analysis; graphene oxide; X-ray absorption fine structure

Beilstein J. Nanotechnol. **2025**, *16*, 1082–1087.

<https://doi.org/10.3762/bjnano.16.79>

Received: 10 February 2025

Accepted: 06 June 2025

Published: 10 July 2025

This article is part of the thematic issue "Fabrication, surface engineering and applications of new materials".

Guest Editor: S. K. Tiwari



© 2025 Entani et al.; licensee Beilstein-Institut.
License and terms: see end of document.

Abstract

Graphene oxide (GO) is expected to be one of the most promising adsorbents for metal ions, including radioactive nuclides in aqueous solutions. Large-area and single-layer graphene oxide (SLGO) grown on α -Al₂O₃(0001) was used as a model structure of GO since the aggregation and re-stacking of the GO sheets prevent the adequate analysis of the adsorption state. The SLGO film was obtained by oxidizing monolayer graphene grown by metal-free chemical vapor deposition on the α -Al₂O₃(0001) surface, and the adsorption state was determined by surface analytical techniques. It was clarified that Cs adsorbs on oxygen functional groups by substituting with H atoms from carboxyl and hydroxy groups. It is also estimated that the weight adsorption capacity of SLGO in the 1.0 mol/L-Cs aqueous solution is as much as approximately 70 wt %. It has been demonstrated that GO has great potential to be a promising adsorbent for Cs in aqueous solutions.

Introduction

Graphene oxide (GO) is oxidized graphene and its surface and periphery are partially modified by epoxy, hydroxy, and carboxy functional groups [1,2]. GO can be thinned to a monolayer of one carbon atom and has a high level of water affinity. Consequently, GO can be expected to have a wide range of applications, such as primers, thermally conductive materials, transparent electrodes, and adsorbent materials [3-13]. GO is

typically synthesized by oxidizing graphite. Several methods have been reported, including the Brodie and Hummers methods, contingent upon the oxidizing agent employed [8,14,15]. GO possesses the ultimate large surface area, low-cost production, and high chemical stability. Therefore, GO has a potential prospect to be an efficient adsorbent for metal ions from aqueous solutions. In order to realize its application use, it

is necessary to form large-area GO films with well-controlled thickness. However, the conventional methods for the fabrication of such tailored GO films present considerable challenges. Conventionally, GO films are obtained by a drop-casting technique, wherein GO flakes dispersed in a solvent are cast onto a substrate [16,17]. This technique does not allow for the control of number of layers.

Consequently, studies have been conducted to synthesize large-area and single-layer GO (SLGO) films. As mentioned above, GO films have typically been fabricated through casting small pieces of GO flakes onto a substrate. In this study, the SLGO film was synthesized by oxidizing single-layer graphene (SLG) grown by metal-free chemical vapor deposition (CVD) on a α -Al₂O₃(0001) substrate. The strong interface interaction between SLG and α -Al₂O₃(0001) can minimize peeling off of SLG from the α -Al₂O₃(0001) substrate following the oxidation process [18]. This allows us to obtain a large-area SLGO film, which can then be subjected to evaluation of the adsorption properties.

Subsequent to the synthesis of SLGO/ α -Al₂O₃(0001), further studies were conducted into its adsorption properties. A significant accident at a nuclear facility can result in the release of substantial amounts of radioactive cesium (Cs) and strontium (Sr) into the environment [19,20]. The development of a method for reducing the volume of these radioactive waste is imperative. Cs and Sr exhibit strong adsorption to particles of rocks and soils, resulting in their water insolubility and substantial volume. A viable method for the disposal of radioactive waste is the application of an acid treatment, which has been demonstrated to be effective in the efficient separation of radioactive Cs contaminants from rocks and soils [21]. The resulting solution is a substantial quantity of low-level radioactive treated water. Therefore, the adsorbent needs to possess high-adsorption performance, a rapid reaction rate, and cost-effectiveness in production. Romanchuk et al. have demonstrated that GO is effective in the removal of actinides from nuclear wastewaters [8]. However, the adsorbing mechanism of metal ions to the GO surface, such as adsorption sites, remains to be elucidated. It has been demonstrated that GO tends to aggregate during the process of metal ion adsorption [8], which complicates the evaluation of GO using surface analytical techniques. The SLGO film synthesized in this study is adhered to the α -Al₂O₃(0001) surface, which prevents GO aggregation and multilayer stacking. It is expected that this will enable detailed evaluation of Cs adsorption on GO.

In this study, the SLGO surface after Cs adsorption was analyzed by surface analytical tools. This enabled us to elucidate the adsorbing sites and electronic state of Cs on SLGO.

Additionally, we examined the electronic structure of Cs adsorbed on SLGO in several different solutions with pH values of 4, 7, and 9. Both the electronic structure and the normalized amount of Cs adsorbates were dependent on the pH scale. These fundamental aspects provide us important information for developing new adsorbent materials using GO.

Results and Discussion

Large-area and single-layer graphene oxide growth

Figure 1 shows an atomic force microscopy (AFM) image of SLG and SLGO on α -Al₂O₃(0001) substrates. The as-grown SLG film has an atomically flat surface and wrinkles with its height less than 0.4 nm [18]. The single layer of graphene was confirmed through X-ray photoelectron spectroscopy (XPS) peak intensity analysis and profiles of normal-incidence X-ray standing wave (NIXSW) spectroscopy [18]. In the SLGO film, the wrinkles disappeared and the surface roughness increased. The root mean square surface roughness (RMS) of the SLGO film is estimated to be less than 0.13 nm. The changes of the local structure are confirmed by Raman spectroscopy measurements. Figure 2 shows two sets of the Raman spectra of SLG and SLGO. In SLG/ α -Al₂O₃(0001), four prominent peaks are identified, which are assigned to the D band (around 1355 cm⁻¹), G band (around 1585 cm⁻¹), 2D band (around 2700 cm⁻¹), and D+G band (around 2900 cm⁻¹). The presence of intense D and D+G peaks is indicative of the existence of graphene film disorder. This phenomenon can be attributed to the reduced size of the graphene grains that are produced at lower growth temperatures [18]. Following the oxidation process, a broadening of all peaks is observed, accompanied by a substantial decrease in the intensity of the 2D band. These alterations are attributed to the presence of defects and a decline

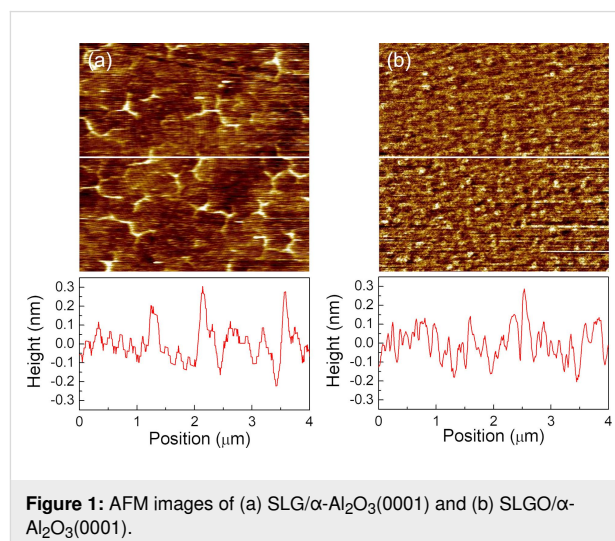


Figure 1: AFM images of (a) SLG/ α -Al₂O₃(0001) and (b) SLGO/ α -Al₂O₃(0001).

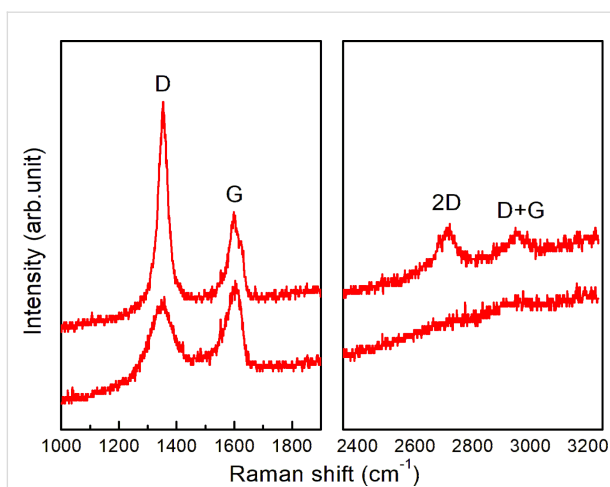


Figure 2: Two sets of Raman spectra from SLG/ α -Al₂O₃(0001) (upper) and SLGO/ α -Al₂O₃(0001) (lower).

in crystallinity, which is associated with the attachment of oxygen functional groups. These spectral features were consistent with the findings reported in [22].

At the same time, the significant changes arose after the oxidization of SLG in the C 1s core XPS and C K-edge near-edge X-ray absorption fine structure (NEXAFS) spectra. Figure 3a shows C 1s XPS spectra of SLG and SLGO. In SLG, an intense peak is observed at 283.4 eV. The C 1s XPS spectra of SLG/ α -Al₂O₃(0001) is shifted to the lower binding energies by 1.0 eV compared with that of graphite (284.4 eV) [23]. This is due to p-type doping of SLG associated with a strong electrostatic interaction between SLG and the α -Al₂O₃(0001) at the interface [18]. In SLGO, on the other hand, a broad structure

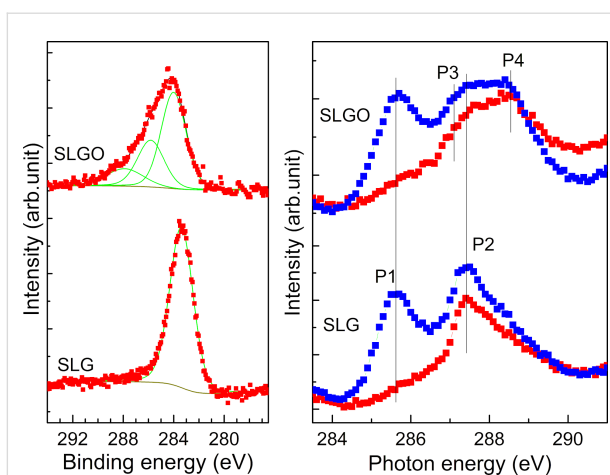


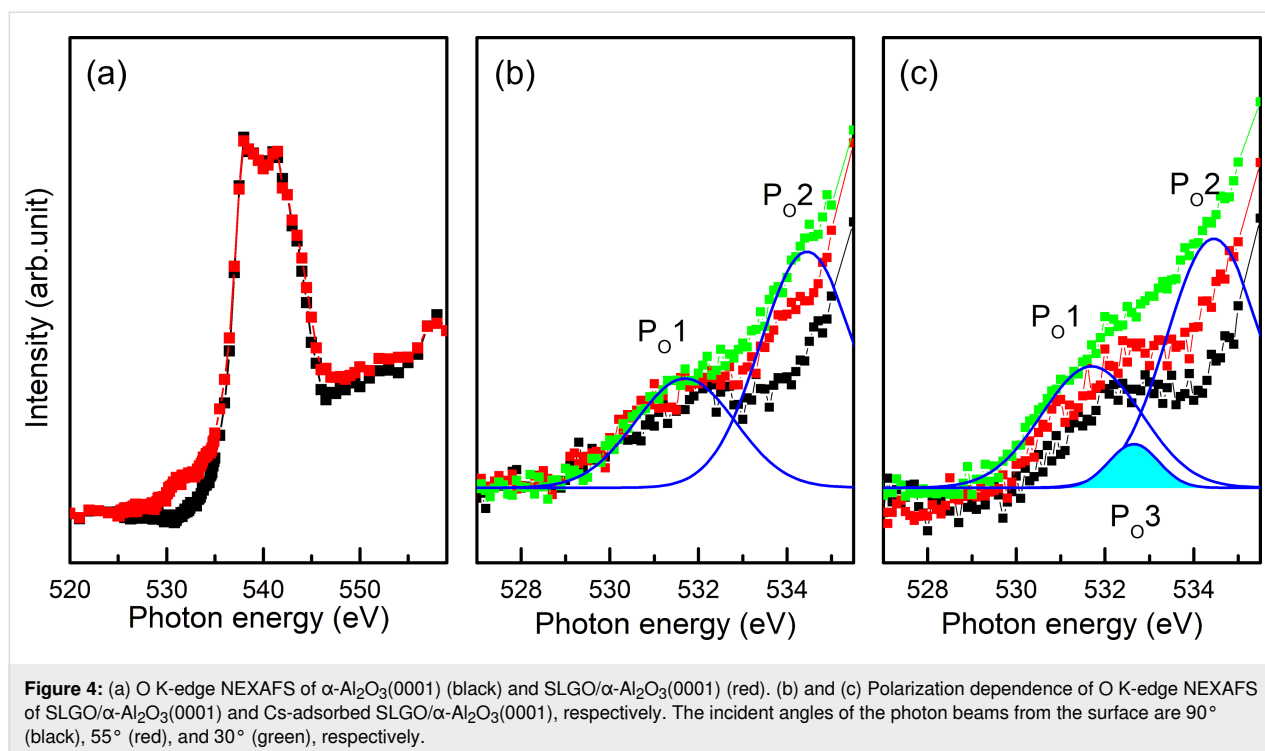
Figure 3: (a) C 1s core level XPS and (b) polarization dependence of C K-edge NEXAFS spectra of SLG/ α -Al₂O₃(0001) (lower) and SLGO/ α -Al₂O₃(0001) (upper). The incident angles of photon beams from the surface are 90° (red) and 30° (blue), respectively.

arose in the higher binding energy region of the intense peak. The structure is originated from the introduction of the oxygen functional groups such as hydroxy and carbonyl groups [24]. It can be reasonably considered that the introduction of the local structures in SLGO causes the relaxation of the interfacial strains and the disappearance of wrinkles as seen in Figure 1b. Figure 3b shows the C K-edge NEXAFS spectra of SLG and SLGO. Two peaks P1 and P2 are observed at 285.4 eV and 287.5 eV. These peaks are assigned to the C 1s to $\pi^*(\text{C}=\text{C})$ and to $\sigma^*(\text{C}-\text{H})$ transitions, respectively [25]. The intensity of P1 at the grazing incidence is much larger than that at the normal incidence. This indicates that the graphene sheet is parallel to the substrate surface. Two additional small features arose in SLGO; 287.1 eV (P3) and 288.4 eV (P4). These are assigned to C 1s to $\pi^*(\text{C}-\text{OH})$ and to $\sigma^*(\text{C}=\text{O})$ transitions, respectively [26–28]. It is also found that P3 and P4 show no X-ray incident angle dependence, which suggests that oxygen functional groups attached to graphene have no particular orientation distribution.

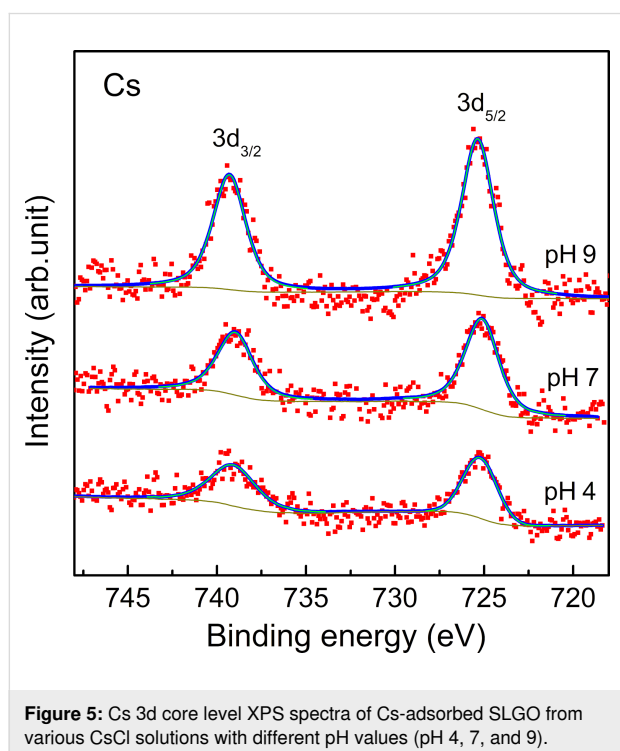
Cs adsorption

The electronic structure of Cs-adsorbed SLGO was also observed by employing NEXAFS. Figure 4a shows the O K-edge NEXAFS spectra of the α -Al₂O₃(0001) substrate and SLGO/ α -Al₂O₃(0001). A pronounced structure is observed at around 540 eV. This structure is originated from the Al–O in the α -Al₂O₃(0001) substrate [29,30]. After the SLGO growth, a small shoulder arises in the lower photon energies. Spectral analysis of this structure shown in Figure 4b indicates that the shoulder consists of two components; P_{O1} (531.6 eV) and P_{O2} (534.4 eV). These are assigned to $\pi^*(\text{O}=\text{C}$ from the carboxyl groups) and $\sigma^*(\text{O}-\text{H}$ from the hydroxyl groups), respectively [23]. It is found that the intensity of P_{O2} shows an incident angle dependence (i.e., the peak intensity measured at the grazing incidence is slightly larger than that at the normal incidence). This indicates that the O–H bond is oriented roughly along the normal direction to the substrate. In the O K-edge spectrum of Cs-adsorbed SLGO shown in Figure 4c, a new component appears at the photon energies between P_{O1} and P_{O2}; P_{O3} (532.7 eV). As detailed in the following section, Cs has been found to be adsorbed on oxygen functional groups through the process of ion exchange. Consequently, it can be inferred that P_{O3} is associated with the O–Cs bonds. It should be noted that the intensity of P_{O3} measured at grazing incidence is slightly larger than that at normal incidence. This indicates that the O–Cs bond tends to be oriented along the normal direction to the SLGO sheet.

For the purpose of elucidating the adsorbing mechanism of the Cs atoms to the SLGO sheet, we investigated the electronic structure and chemical properties of adsorbed Cs by changing



the pH level of the Cs aqueous solutions. Figure 5 shows Cs 3d XPS spectra of Cs-adsorbed SLGO under three different pH values. No energy shift was observed among these spectra. This indicates that the chemical state of adsorbed Cs is identical regardless of the pH value. In contrast, it should be noted that



the capacity of the Cs adsorption significantly increases with an increasing pH value. It has been reported that the oxygen functional groups in GO have dissociation constants $pK = 4.3, 6.6,$ and 9.8 [31]. It can be considered that Cs adsorbs on the oxygen functional groups through a mechanism of ion exchange. This process involves the substitution of H atoms from oxygen functional groups, such as carboxyl and hydroxy groups, with Cs atoms. It can therefore be surmised that the ability of SLGO for the Cs adsorption is significantly decreased in strong acid aqueous solutions due to the suppression of hydrogen dissociation from oxygen functional groups in SLGO. It is claimed that the pH value of the aqueous solution should be maintained at neutrality and/or alkalinity for the efficient Cs adsorption by SLGO. With regard to the quantitative analysis, it is also noted that SLGO shows high adsorption capacity of Cs. That is, the weight adsorption capacity in the CsCl solution with pH 7 is estimated to be 650–850 mg Cs per 1 g SLGO, which corresponds to 70 wt %, from the XPS analysis based on the peak intensity ratio between C 1s and Cs 3d. This value is considerably higher than that of existing adsorbents, including zeolite ($189 \text{ mg}\cdot\text{g}^{-1}$) [32–34]. GO is comprised of light elements, which results in a significantly high calculated adsorption capacity.

Conclusion

In this study, the synthesis of the large-area SLGO film was accomplished through the oxidation of CVD-grown SLG/ $\alpha\text{-Al}_2\text{O}_3(0001)$. We found that the change in the electronic state from graphene to GO is attributed to oxidation. This was

accompanied by the decrease of the $\pi^*(C=C)$ state and the appearance of states derived from oxygen functional groups. Subsequently, the adsorption mechanism of Cs on GO was investigated using SLGO/ α -Al₂O₃(0001) as the model structure. It was found that Cs adsorbs on SLGO by the substitution of H from oxygen functional groups, such as carboxyl and hydroxy groups. It was also indicated that SLGO shows the high Cs adsorption capacity of 650–850 mg·g⁻¹ in the 1.0 mol/L-Cs aqueous solution. SLGO adsorbs Cs via hydrogen exchange, resulting in an accelerated adsorption rate and a higher weight adsorption capacity compared to existing adsorbents, including zeolites. Consequently, SLGO was demonstrated to be a promising adsorbent. As SLGO grown on α -Al₂O₃(0001) exhibits stable adhesion to the substrate and possess a large surface area, we are interested in exploring a broad spectrum of potential applications. These applications may include sensing materials and primers in addition to adsorbents, which could be investigated in future research.

Experimental

Growth of SLGO on α -Al₂O₃(0001)

SLGO was grown by a method analogous to [35]. Before synthesizing SLGO, SLG was grown on an α -Al₂O₃(0001) substrate (size: 10 × 10 mm², thickness: 430 μ m). The substrate was annealed at 900 °C in open air in order to obtain an atomically flat surface. Then, the substrate was introduced into a vacuum furnace. The base pressure of the furnace was 6 × 10⁻⁶ Pa. After evacuating, the substrate was annealed up to 1000 °C for 1 h. For the graphene growth, a methanol vapor was used as a precursor. The SLG was grown by introducing 200 Pa methanol vapor for 30 min [18]. The single layer of graphene was inspected by the intensity analysis of XPS and the profiles of NIXSW for graphene/ α -Al₂O₃(0001). After the SLG growth, the SLG in the sample was oxidized based on the modified Hummers method [24]. The procedure was as follows: The mixture of H₂SO₄ and KMnO₄ was prepared by slowly adding KMnO₄ (1.8 g) into concentrated H₂SO₄ (20 mL) and stirring in the beaker. SLG/ α -Al₂O₃(0001) was dipped in the mixture for 30 s. The oxidized specimen was washed with purified water and dried under nitrogen gas blow.

Cs adsorption

Prior to Cs adsorption, the SLGO surface was treated with aqueous solutions which were adjusted to pH 4, 7, and 9 prior to the adsorption of the Cs atoms. Solutions with pH values of 4 and 9 were adjusted with acetate and borate buffer solutions, respectively. Then the SLGO surface was dipped into a 1.0 mol/L CsCl solution with the same pH values. The solutions were kept at room temperature. Both pH adjustment and CsCl solutions were added dropwise on the SLGO surface. The volumes of the solutions and contact times were 1 μ L and 5 min, respectively.

After Cs adsorption, the CsCl solution was removed with a water rinse for 5 min.

Characterization

The electronic structure of Cs-adsorbed SLGO was investigated by NEXAFS. The C and O K-edge NEXAFS measurements were carried out at the BL-8 station in the Ritsumeikan Synchrotron Radiation Center. The partial electron-yield method was employed to obtain the spectra. The amount of Cs adsorption was inspected by XPS. The energy scan for XPS was done with a VSW CLASS 100 hemispherical energy analyzer. An Al K α (1486.6 eV) X-ray source (PSP TX400/2) was used for the excitation. In the XPS measurement, the CsCl solution was removed from the SLGO surface by water rinsing and then the Cs-adsorbed SLGO specimen was introduced in the XPS chamber kept at ultra-high vacuum. The surface morphology of SLGO was examined using atomic force microscopy (AFM, SII SAP300).

Funding

The present work was supported in part by the KAKENHI Grant-in-aid for Scientific Research (C) JP23K04549.

Author Contributions

Shiro Entani: conceptualization; investigation; writing – original draft. Mitsunori Honda: investigation. Masaru Takizawa: investigation. Makoto Kohda: supervision.

ORCID® iDs

Shiro Entani - <https://orcid.org/0000-0001-9062-1123>

Makoto Kohda - <https://orcid.org/0000-0002-1995-1282>

Data Availability Statement

All data that supports the findings of this study is available in the published article and/or the supporting information of this article.

References

- He, H.; Klinowski, J.; Forster, M.; Lerf, A. *Chem. Phys. Lett.* **1998**, *287*, 53–56. doi:10.1016/S0009-2614(98)00144-4
- Dikin, D. A.; Stankovich, S.; Zimney, E. J.; Piner, R. D.; Dommett, G. H. B.; Evmenenko, G.; Nguyen, S. T.; Ruoff, R. S. *Nature* **2007**, *448*, 457–460. doi:10.1038/nature06016
- Jia, S.; Sun, H. D.; Du, J. H.; Zhang, Z. K.; Zhang, D. D.; Ma, L. P.; Chen, J. S.; Ma, D. G.; Cheng, H. M.; Ren, W. C. *Nanoscale* **2016**, *8*, 10714–10723. doi:10.1039/c6nr01649a
- Chen, J.; Li, L. J. *Mater. Res. Technol.* **2020**, *9*, 13740–13748. doi:10.1016/j.jmrt.2020.09.092
- Mallikarjuna, K.; Kim, H. *ACS Appl. Mater. Interfaces* **2019**, *11*, 1969–1978. doi:10.1021/acsami.8b14086
- Wang, Y.; Wang, F.; Wang, H.; Song, M. *Sci. Rep.* **2017**, *7*, 16510. doi:10.1038/s41598-017-16836-x
- Mu, X.; Wu, X.; Zhang, T.; Go, D. B.; Luo, T. *Sci. Rep.* **2014**, *4*, 3909. doi:10.1038/srep03909

8. Romanchuk, A. Y.; Slesarev, A. S.; Kalmykov, S. N.; Kosynkin, D. V.; Tour, J. M. *Phys. Chem. Chem. Phys.* **2013**, *15*, 2321. doi:10.1039/c2cp44593j
9. Sitko, R.; Turek, E.; Zawisza, B.; Malicka, E.; Talik, E.; Heimann, J.; Gagor, A.; Feist, B.; Wrzalik, R. *Dalton Trans.* **2013**, *42*, 5682. doi:10.1039/c3dt33097d
10. Chen, S.; Hong, J.; Yang, H.; Yang, J. J. *Environ. Radioact.* **2013**, *126*, 253–258. doi:10.1016/j.jenvrad.2013.09.002
11. Yang, S.-T.; Chang, Y.; Wang, H.; Liu, G.; Chen, S.; Wang, Y.; Liu, Y.; Cao, A. J. *Colloid Interface Sci.* **2010**, *351*, 122–127. doi:10.1016/j.jcis.2010.07.042
12. Zhao, G.; Ren, X.; Gao, X.; Tan, X.; Li, J.; Chen, C.; Huang, Y.; Wang, X. *Dalton Trans.* **2011**, *40*, 10945–10952. doi:10.1039/c1dt11005e
13. Entani, S.; Honda, M.; Shimoyama, I.; Li, S.; Naramoto, H.; Yaita, T.; Sakai, S. *Jpn. J. Appl. Phys.* **2018**, *57*, 04FP04. doi:10.7567/jjap.57.04fp04
14. Brodie, B. C. *Ann. Chim. Phys.* **1960**, *59*, 466–472.
15. Hummers, W. S., Jr.; Offeman, R. E. *J. Am. Chem. Soc.* **1958**, *80*, 1339. doi:10.1021/ja01539a017
16. Sun, P.; Ma, R.; Wang, K.; Zhong, M.; Wei, J.; Wu, D.; Sasaki, T.; Zhu, H. *Nanotechnology* **2013**, *24*, 075601. doi:10.1088/0957-4484/24/7/075601
17. Lim, W.; Yap, Y.; Chong, W.; Ahmad, H. *Sensors* **2014**, *14*, 24329–24337. doi:10.3390/s141224329
18. Entani, S.; Antipina, L. Y.; Avramov, P. V.; Ohtomo, M.; Matsumoto, Y.; Hirao, N.; Shimoyama, I.; Naramoto, H.; Baba, Y.; Sorokin, P. B.; Sakai, S. *Nano Res.* **2015**, *8*, 1535–1545. doi:10.1007/s12274-014-0640-7
19. Yasunari, T. J.; Stohl, A.; Hayano, R. S.; Burkhart, J. F.; Eckhardt, S.; Yasunari, T. *Proc. Natl. Acad. Sci. U. S. A.* **2011**, *108*, 19530–19534. doi:10.1073/pnas.1112058108
20. Tanaka, K.; Sakaguchi, A.; Kanai, Y.; Tsuruta, H.; Shinohara, A.; Takahashi, Y. *J. Radioanal. Nucl. Chem.* **2013**, *295*, 1927–1937. doi:10.1007/s10967-012-2160-9
21. Yasutaka, T.; Kwamoto, T.; Komai, T. *Radioisotopes* **2013**, *62*, 211–218. doi:10.3769/radioisotopes.62.211
22. Yang, D.; Velamakanni, A.; Bozoklu, G.; Park, S.; Stoller, M.; Piner, R. D.; Stankovich, S.; Jung, I.; Field, D. A.; Ventrice, C. A., Jr.; Ruoff, R. S. *Carbon* **2009**, *47*, 145–152. doi:10.1016/j.carbon.2008.09.045
23. Hamrin, K.; Johansson, G.; Gelius, U.; Nordling, C.; Siegbahn, K. *Phys. Scr.* **1970**, *1*, 277–280. doi:10.1088/0031-8949/1/5-6/018
24. Lerf, A.; He, H.; Forster, M.; Klinowski, J. *J. Phys. Chem. B* **1998**, *102*, 4477–4482. doi:10.1021/jp9731821
25. Kikuma, J.; Yoneyama, K.; Nomura, M.; Konishi, T.; Hashimoto, T.; Mitsumoto, R.; Ohuchi, Y.; Seki, K. *J. Electron Spectrosc. Relat. Phenom.* **1998**, *88–91*, 919–925. doi:10.1016/s0368-2048(97)00220-x
26. Pacilé, D.; Meyer, J. C.; Fraile Rodríguez, A.; Papagno, M.; Gómez-Navarro, C.; Sundaram, R. S.; Burghard, M.; Kern, K.; Carbone, C.; Kaiser, U. *Carbon* **2011**, *49*, 966–972. doi:10.1016/j.carbon.2010.09.063
27. Jeong, H.-K.; Noh, H.-J.; Kim, J.-Y.; Jin, M. H.; Park, C. Y.; Lee, Y. H. *EPL* **2008**, *82*, 67004. doi:10.1209/0295-5075/82/67004
28. Kuznetsova, A.; Popova, I.; Yates, J. T., Jr.; Bronikowski, M. J.; Huffman, C. B.; Liu, J.; Smalley, R. E.; Hwu, H. H.; Chen, J. G. *J. Am. Chem. Soc.* **2001**, *123*, 10699–10704. doi:10.1021/ja011021b
29. Horiuchi, S.; Liu, Y.; Hanada, T.; Akiyama, H. *Appl. Surf. Sci.* **2022**, *599*, 153964. doi:10.1016/j.apsusc.2022.153964
30. Frati, F.; Hunault, M. O. J. Y.; de Groot, F. M. F. *Chem. Rev.* **2020**, *120*, 4056–4110. doi:10.1021/acs.chemrev.9b00439
31. Konkena, B.; Vasudevan, S. J. *J. Phys. Chem. Lett.* **2012**, *3*, 867–872. doi:10.1021/jz300236w
32. Yang, H.; Sun, L.; Zhai, J.; Li, H.; Zhao, Y.; Yu, H. J. *Mater. Chem. A* **2014**, *2*, 326–332. doi:10.1039/c3ta13548a
33. Al Abdullah, J.; Al Lafi, A. G.; Al Masri, W.; Amin, Y.; Alnama, T. *Water, Air, Soil Pollut.* **2016**, *227*, 241. doi:10.1007/s11270-016-2938-4
34. Johan, E.; Yoshida, K.; Munthali, M. W.; Matsue, N.; Itagaki, Y.; Aono, H. J. *Ceram. Soc. Jpn.* **2015**, *123*, 1065–1072. doi:10.2109/jcersj2.123.1065
35. Takaoka, K.; Mitsuhara, K.; Takizawa, M.; Entani, S.; Sakai, S. *e-J. Surf. Sci. Nanotechnol.* **2018**, *16*, 320–323. doi:10.1380/ejsnt.2018.320

License and Terms

This is an open access article licensed under the terms of the Beilstein-Institut Open Access License Agreement (<https://www.beilstein-journals.org/bjnano/terms>), which is identical to the Creative Commons Attribution 4.0 International License (<https://creativecommons.org/licenses/by/4.0>). The reuse of material under this license requires that the author(s), source and license are credited. Third-party material in this article could be subject to other licenses (typically indicated in the credit line), and in this case, users are required to obtain permission from the license holder to reuse the material.

The definitive version of this article is the electronic one which can be found at:
<https://doi.org/10.3762/bjnano.16.79>



Missing links in nanomaterials research impacting productivity and perceptions

Santosh K. Tiwari^{*1} and Nannan Wang²

Perspective

Open Access

Address:

¹Centre for New Materials and Surface Engineering, Department of Chemistry, NMAM Institute of Technology (NMAMIT), Nitte (Deemed to be University), Nitte 574110, Karnataka, India and ²State Key Laboratory of Featured Metal Materials and Life-cycle Safety for Composite Structures, School of Resources, Environment and Materials, Guangxi University, Nanning, Guangxi 530004, China

Email:

Santosh K. Tiwari^{*} - ismgraphene@gmail.com

^{*} Corresponding author

Keywords:

commercialization; nanomaterials; public-facing technologies; standardization; translational barriers

Beilstein J. Nanotechnol. **2025**, *16*, 2168–2176.

<https://doi.org/10.3762/bjnano.16.149>

Received: 23 June 2025

Accepted: 18 November 2025

Published: 03 December 2025

This article is part of the thematic issue "Fabrication, surface engineering and applications of new materials".

Associate Editor: X. Song



© 2025 Tiwari and Wang; licensee Beilstein-Institut.
License and terms: see end of document.

Abstract

Herein we point out critical yet often overlooked barriers restraining the real-world impact and commercial viability of nanomaterials research. In spite of decades of scientific progress, nanotechnology remains underutilized in public-facing applications. A major issue is the limited engagement of leading tech industries in developing nanotechnology-based products, prompting concerns about tangible societal and industrial outcomes. Far away, funding challenges, the field is hindered by fragmented regulations, ambiguous safety guidelines designed for bulk materials, and the absence of globally harmonized standards. These systemic limitations, coupled with persistent misconceptions, have stalled translation from lab to market. In contrast to numerous productive technologies like generative AI, machine learning, and related progress, nanotechnology has not achieved autonomous societal integration. The author argues that without a unified, transparent, and science-driven global regulatory framework, the transformative potential of nanotechnology will remain unrealized, despite over decades of excellent discoveries. This perspective calls for carefully considerations linked to productivity perception, true funding utility, and foundational reform to unlock nanotechnology's full promise across sectors.

Perspective

Atom-by-atom innovation

The historical creation of nanomaterials and their applications is much older than often assumed and has long been a subject of debate. It would be wrong to believe that nanomaterials have been utilized only within the last century. In fact, several

remarkable works and historical examples are well documented and discussed in the literature [1-3]. But the true turning point for nanoscience came in 1959, when physicist Richard Feynman delivered his seminal lecture, "There's Plenty of

Room at the Bottom”, at the annual meeting of the American Physical Society at Caltech, USA. This lecture provided a visionary perspective that inspired generations of researchers and greatly accelerated systematic investigations in producing and exploiting nanoscale materials. Although it took decades for technology to catch up with his ideas, his foresight catalyzed a profound shift in the way scientists approached the material world. What was once philosophical became increasingly feasible and eventually tangible. Since then, various aspects of nanoscience and nanotechnology have evolved, ranging from the examination of unique nanostructures, nanoscale characterization, metrology to nanoelectronics, nanophotonics, nanobiotechnology, nanomedicine, nanofabrication, and nanomanufacturing [4,5]. These new developments catalyzed the initiation of numerous new experimental and theoretical areas in different branches of science and engineering. Importantly, all of these studies are directly related to the creation of nanomaterials aimed at delivering much higher efficiency for specific applications compared to their conventional counterparts. In this way, progress in nanomaterial research has seen a remarkable acceleration after the discovery of fullerene by Kroto and co-workers in 1985 and witnessed an even more rapid surge following the discovery of graphene and the award of the Physics Nobel Prize in 2010 [6,7].

Graphene is often referred to as a “wonder material” due to its seemingly infinite potential in almost every domain of science and technology [8]. Its exceptional thermo-mechanical properties are ideal for critical sectors such as aerospace, medicine, space exploration, textiles, construction, and materials capable of operating from cryogenic temperatures up to beyond 2000 °C [8,9]. Similarly, other 2D nanomaterials, such as elemental 2D materials (e.g., borophene, phosphorene, and silicene), transition metal dichalcogenides (e.g., MoS₂, WS₂, and NbSe₂), transition metal oxides (e.g., MnO₂, Fe₂O₃, and Ni(OH)₂ nano-sheets), MXenes (e.g., Ti₃C₂, Ti₂C, and Ta₄C₃), 2D halides (e.g., CrI₃, NiI₂, and FeCl₂), 2D nitrides (e.g., BCN), 2D transition metal nitrides (e.g., MoN, Ti₄N₃, and GaN) [10], 2D carbides (e.g., α -C₂N and B₂C), 2D perovskites (e.g., (BA)₂PbI₄), and 2D metal-organic frameworks have also shown extraordinary promise. These nanosystems exhibit exceptional physical and chemical properties, with electronic and quantum mechanical behaviors that continue to surprise the scientific community [11]. Researchers are continuously developing and reporting new nanomaterials with unique properties tailored for diverse applications. Thus, the properties of materials once considered impossible are now accessible for real-world technological applications. In addition, nanoscience has initiated several new areas in fundamental physics and molecular dynamics, representing a profound scientific achievement of the 21st century [12]. It is noteworthy that these developments have

strongly reinforced extensive collaborative and multidisciplinary research efforts around the world. Thus, at present, chemists, physicists, biologists, engineers, and computer scientists are working more closely together than ever before to design, synthesize, and apply nanosystems. Authors consider this to be one of the most important achievements in the history of science. The influence of nanomaterials research goes beyond academic curiosity. It has triggered the evolution of microscopic and analytical techniques to visualize matter at unprecedented spatial and temporal resolution, to the point where we can now visualize materials at molecular and atomic scales with unprecedented resolution. Without the demands of nanomaterials research, such advancements in instrumentation and methodology would likely have taken much longer to emerge. Notably, nanomaterial research not only has expanded the technological frontier, but has also reshaped our philosophical understanding of materials. It challenges human cognition to imagine the real-world implications of manipulating matter atom by atom. What was once the domain of speculative science fiction materials that self-heal, adapt, respond, or compute is now increasingly feasible. The boundaries between the natural and artificial, between living and nonliving systems, are being redefined through materials engineered at the nanoscale. It is important to elucidate that authors do not intend a direct comparison between nanotechnology and the fields such as generative AI, machine learning, and related progress. The latter areas are inherently multidisciplinary, encompassing multiple research domains, with nanotechnology often representing only a component. Nevertheless, from a user-oriented perspective, generative AI, machine learning, and Internet of Things are experiencing rapid growth and receiving substantial funding with relatively few obstacles. In contrast, nanotechnology and nanomaterials research remains largely fundamental in nature, which contributes to comparatively lower levels of funding. Therefore, it would be incorrect to assume that nanotechnology has received extensive financial support and efforts but yielded limited outputs. In reality, this perception persists primarily within academic and industrial circles due to the fundamental and exploratory character of nanoscience and nanotechnology.

Commercial adoption and mass usage remain uncertain

As discussed above, during the last three decades, extensive work has been done in various domains of nanoscience and nanotechnology, mainly focusing on large-scale production and potential consumer applications. It is estimated that, globally, investments in nanomaterials and broader nanotechnology over this period have ranged from half a trillion to nearly one trillion US dollars, roughly \$400 billion from government sources and a comparable amount from industry [13–15]. Moreover, on the

basis of data indexed in Web of Science and Scopus, it is evident that carbon nanotubes, graphene, metal oxides, quantum dots, and MXenes are among the most extensively studied and explored nanomaterials. These materials have been researched in nearly every discipline, leading to the establishment of numerous startups and companies focused on their production, processing, and innovative applications (Table 1). Nevertheless, in the face of such massive research efforts and innovation, widespread application and commercialization of these advanced materials remain limited [16]. The use of nanomaterials is largely confined to selected new technologies and niche innovations, with very little penetration into everyday public life. This stark gap highlights a sobering reality: Even after decades of research and good funding, the real-world integration and due consumption of nanomaterials are still minimal. When we compare the return on investment and impact with other technological revolutions such as generative AI, machine learning, Internet of Things, and related progress, nanotechnology falls short in terms of commercial and practical outcomes. It is understandable that nanotechnology is still an emerging field that is inherently more exploratory in nature. In other words, though nanomaterials research has made impressive scientific advances, its translation into mass-market products remains partial. Therefore, it raises a vital and valid question: Why are heavily researched nanomaterials such as carbon nanotubes, graphene, metal oxides, quantum dots, and MXenes still so underutilized? Surprisingly, many of us working on nanomaterials often believe that materials such as graphene, quantum dots, and MXenes are widely used in various engineering and domestic products; however, this is a misconception. The contribution of these new materials, even to cutting-edge technologies, currently is very little in commercial products. Over the past 14 years of working on these new materials, collaborating internationally, engaging with admired scientists and professors, and now leading my own research group, Santosh K. Tiwari identified a number of key reasons for underproductivity in nanotechnology. Of course, it is the author's personal observation, but they are grounded in data and real-world experience, mostly through discussions with industry partners.

First, if we carefully examine the educational backgrounds and training of academics, scientists, engineers, and research personnel working extensively in various aspects of nanotechnology, we find that the majority come from chemistry, physics, materials science, and metallurgy. Very few come from other fields such as mechanical, energy, electronics, biomedical engineering, and mathematics. The experts belonging to chemistry, physics, and metallurgy background have been exceptional at understanding and uncovering fundamental insights into nanomaterials. They have pioneered breakthroughs and developed most of the essential tools required to industrialize nanomaterial-

al-based products. However, they have largely not focused on the commercialization of these advancements. As a result, only a few companies are currently utilizing the potential of nanomaterials by training their workforce accordingly (Table 1). To overcome this gap, we need globally structured and domain-specific educational programs in nanoengineering, starting from secondary school through to undergraduate levels. Such specialized courses remain extremely rare worldwide. Though it is true that nanotechnology-related graduate degrees are offered globally, but most are either too broad or overly interdisciplinary, which often dilutes the focus and intent of the training. Authors, believe that engineers trained specifically in nanomaterials and nanotechnology would become valuable assets in driving innovation and entrepreneurship in this field. The authors also claim these curricula not only be domain-specific, but also include modules on manufacturing, entrepreneurship, and regulatory aspects. The regulatory aspects of nanotechnology are a complex issue worldwide. Collaboration between academia and industry in the design of these programs would ensure relevance. Early education from secondary school onwards can foster interest and build a skilled workforce ready for the nanotechnology-driven future. Meanwhile, interdisciplinary researchers can continue to push the frontiers of fundamental knowledge and discovery.

Second, most nanotechnology-related products are found in big tech industries (Table 1) including space, biomedicine, and agriculture, and do not produce instantaneous and dramatic impacts that a nonscientific audience can easily perceive, unlike developments in AI, virtual reality, or other highly visible innovations. This lack of immediate, observable transformation has contributed to a strong perception, especially among political leaders, policymakers, and regulatory authorities, that nanomaterials are more of a scientific hype than practical reality [17]. As a result, there is limited motivation among these groups to actively promote and implement nanotechnology advances in public domains. Instead, they tend to continue satisfying societal needs with conventional products, which appear to be "good enough" in their view. In today's world, there are many political figures, such as the President of the US, Mr. Trump, and his administration, who dismissed climate change and CO₂ emissions as irrelevant. Similarly, a substantial portion of leadership at various levels believes that conventional materials are already fulfilling current demands; thus, they see no need to engage with the complexities of adopting entirely new technologies/materials. These officials, even within universities/research organizations, may appreciate research output in the form of publications and patents, but when it comes to translating that research into real-world products, they often withdraw support. This is not necessarily due to a lack of interest in innovation and efficiency, but rather because they are reluctant to engage in the

Table 1: List of well-known global companies and startups driving nanomaterials, nanotechnology products, and devices. Though not exclusively focused on nanotechnology, these organizations remain key players transitioning from conventional bulk materials toward advanced nanoscale innovations.

Company	Origin	Known for
NVIDIA Corp	USA	NVIDIA is most famous for advancing GPUs
Intel	USA	semiconductor devices using advanced nanoscale process nodes
Applied Materials	USA	tools/services for nanoscale device fabrication (equipment)
Samsung Electronics	South Korea	nanoscale memory, quantum dots, and logic devices in consumer electronics
Nanosys	USA	quantum-dot display materials for high-end displays
Evonik	Germany	nanosilica and functional additives for coatings and energy applications
Merck KGaA	Germany	nanomaterials for electronics, life sciences reagents, and display materials
Nanoco	UK	quantum dot materials used in bioimaging and specialty displays (commercial quantum-dot products)
Umicore	Belgium	nanocatalysts and materials for energy/catalysis applications
NAWA Technologies	France	nanotube/nanocarbon products for energy storage and composites
Nanotech Industrial Solutions	Canada	nanolubricants and surface treatment products
Johnson & Johnson	USA	nanoformulation medical products and devices
Log9 Materials	India	graphene-based products including filters and energy devices (aluminium–air solutions)
Graphmatech	Sweden	graphene-enabled additives and composite products
Kastus Technologies	Ireland	photocatalytic antimicrobial coatings that work under visible light for surfaces and touchscreens
Nanjiang Group	China	carbon nanotubes, super-strong nanomaterials, cooperating with universities for industry-applicable nanotechnology products
Naxau New Material Co.	China	nanocoating solutions: wear resistance, corrosion resistance, adjusted conductivity, thermal properties, coatings for automotive, medical, electronics
Imina Technologies	Switzerland	micro-/nano-fluidic devices used in diagnostics

rigorous and often disruptive process of establishing new policies, regulations, and frameworks required to integrate new technologies into existing systems.

Last, almost all major big tech and engineering companies are now well aware of the vast potential of nanomaterials. In fact, many of them actively support and maintain internal research and development (R&D) programs focused on various aspects of nanomaterials. However, because their existing production and engineering infrastructures are heavily optimized for bulk materials, these companies are intentionally avoiding disruptive changes in instrumentation, processing, and manufacturing tools. Of course, the goal such tech companies are to continue to profit from legacy systems, especially since most of their competitors are not yet adopting nanomaterials, although these could offer considerably better performance, sustainability, longevity, and efficiency. The founders, CEOs, and CTOs of such companies are strategically positioning themselves for a future in which the adoption of nanomaterials becomes inevitable and highly competitive. Moreover, some tech giants are already introducing nanomaterial-based products, albeit

very slowly, under the guise of luxury and premium branding (Table 1). This allows them to make larger profits while gradually preparing the market. For example, Apple Inc. and Samsung are well ahead in graphene research for electronic applications [18,19]. However, highly flexible smartphones and advanced graphene-based devices remain limited, exclusive, and mostly in the pipeline. Similarly, Samsung's quantum dot-based smart TV displays are available, but in a controlled and exclusive manner. In essence, business strategy plays a significant role in deliberately delaying the wide release of exceptionally smart and efficient nanomaterial-based products. This scenario echoes historical precedents, such as electric vehicles that were functional in London and New York [20] as early as 1925. Initially, the oil industry effectively suppressed the growth and innovation of EV technology to protect its own interests.

The origin of nanomaterials is the real culprit
Nanomaterials hold immense potential, as highlighted in the preceding discussion. Yet, it is important to note that a very significant percentage of nanomaterials with promising applica-

tions is synthesized in labs. In contrast, naturally occurring nanomaterials are very inadequate in scale and, in most cases, are not practically useful for real-world applications, especially in the context of advanced technologies. In this regard, more than 85% of nanomaterials synthesis and production processes involve the use of hazardous chemicals such as hydrogen cyanide, sulfuric acid, phosphoric acid, nitric acid, hydrochloric acid, sodium hydroxide and potassium hydroxide [21]. To produce nanomaterials, these chemicals are not used in trace amounts but in substantial quantities. During synthesis, nearly 40–50% of these chemicals result in waste, which harms ecological systems by contaminating water, air, and soil, even when strict preventive measures are in place. Moreover, the environmental pollution caused by nanomaterials after their lifecycle, along with the chemicals used in their synthesis, is much more hazardous; up to a thousand times more compared to their bulk counterparts [22]. Additionally, most nanomaterial fabrication methods are energy-intensive. Techniques such as combustion, arc deposition, solvothermal synthesis, chemical vapor deposition, mechanical milling, and wet chemical methods require high energy input and careful process control. The ultrahigh cost of equipment, especially characterization tools used for nanosystems, are unavoidable challenges.

Another critical challenge is the precision required to produce nanomaterials. The unique properties of nanomaterials arise from controlled particle size, but achieving the desired size and uniformity is extremely difficult, even with advanced techniques. Although there are various innovative methods for producing nanomaterials, very few can consistently deliver particles with the desired properties, even under controlled experimental conditions. Therefore, after production, comprehensive characterization of nanomaterials becomes a tedious and expensive task, often more so than for advanced bulk materials. It is indispensable to acknowledge that even after detailed characterization, warranting that even 90% of the nanoparticles have uniform size and identical surface characteristics is difficult. This is largely due to the inherent instability of 0D, 1D, and 2D nanomaterials [23]. That is why, in most cases, nanomaterials require a specific medium and controlled environment for stability. In the same line, due their high surface energy, large surface area, and small size, nanomaterials naturally tend to aggregate, agglomerate, and self-assemble according to their morphology. These issues cannot be fully eliminated without external stabilization and suggestively impact their performance in real-world applications. Furthermore, such an instability becomes more pronounced as the particle size decreases. For instance, quantum dots are excellent nanomaterials, but their practical application is much more challenging compared to particles greater than 20 nm in size.

Authors believe, at present, the scientific community has explored numerous types of nanomaterial, including quantum dots, and has demonstrated their potential in the lab to address technological and societal challenges. Therefore, it is now imperative to shift the focus towards developing green and sustainable synthesis pathways. More importantly, the global scientific community must establish standardized protocols to maximize the positive impact of nanomaterials. These protocols should go over short-sighted strategies like recycling and usage restrictions. Similarly, to how systematic regulations exist for human cell research or radioactive materials, nanomaterial research must also be governed by robust guidelines to prevent uncontrolled proliferation. Otherwise, excessive production of nanomaterials for academic prestige and numerous hit-and-miss experimental works without delivering meaningful benefits may expose humanity to severe health risks, including cancer and other life-threatening diseases [24]. We are fully aware that enforcing such strict rules and close monitoring in nanomaterials research in each lab globally is not easy and may hinder scientific inquiry too. However, the scientific community must reflect on this challenge and work towards developing mutual understanding. In this context, it is worth sincerely noting that direct exposure of such chemicals (nanoscale systems) to the environment is very poorly managed worldwide, with the exception of a few countries, namely the UK, Germany, Sweden, Denmark, Netherlands, and Japan. Furthermore, the interaction of nanomaterials with biological systems remains poorly understood and could potentially lead to fatal genetic mutations.

Funding realities in nanotechnology research

Over the past decade, discussions at major scientific conferences, in scholarly commentaries, and among policymakers have increasingly questioned the tangible returns of decades of investment in nanomaterials and nanotechnology research. This skepticism is principally salient given the substantial public and private funding committed to the field. Although it is partially true that nanotechnology has not always met the high expectations set during the “Nano-Hype” era of the early 2000s, claims that the field has failed to deliver are an oversimplification that misrepresents the nature and trajectory of scientific progress. Since the launch of flagship programs like the US national nanotechnology initiative in 2000, cumulative global investment in nanotechnology R&D has exceeded \$500 billion, though notably less than the often-cited (and inflated) \$1 trillion figure [13–15]. This funding has primarily supported fundamental research across materials science, chemistry, physics, and bioengineering. These efforts have led to major scientific advances, mainly in nanoelectronics, nanomedicine, catalysis, and energy storage. However, many of these contributions are embedded in downstream technologies and applications that are

not always explicitly marketed as “nanotechnology”. As a result, their impact is often undervalued. In contrast, investment only in generative AI has surged dramatically in recent years. As of 2024, global funding in AI including private equity, venture capital, and governmental initiatives has surpassed \$1.5 trillion [25]. This comparison often serves to highlight the perceived disparity in returns between generative AI and nanotechnology. Nonetheless, such a juxtaposition overlooks critical differences in research maturity, regulatory complexity, and commercialization pathways between the two fields.

One underappreciated aspect of nanotechnology funding is the high percentage allocated toward building sophisticated research infrastructure, predominantly in emerging economies. Unlike generative AI where a large portion of funding goes directly into product development and use, nanotechnology, still in a growing and exploratory phase has required considerable investment in physical infrastructure, metrology, safety protocols, and specialized facilities. These investments are necessary prerequisites for long-term innovation but can obscure short-term output metrics. Furthermore, in many countries such as China, India, and Brazil, some share of nanotechnology-related funding has originated from corporate social responsibility (CSR) initiatives, often mandated by government policy. Although such funding adds to the nominal investment figures, it is frequently used to establish buildings and institutional branding rather than driving core scientific innovation and product development. These CSR contributions, especially when tied to tax benefits/political goodwill, rarely undergo rigorous outcome-based auditing. As a result, much of the funding appears in national and institutional reports but contributes marginally to impactful nanotechnology outputs. A key telling example can be seen in private universities and R&D centers established by almost every large business conglomerate in countries like India. These institutions often function as vehicles for CSR spending and tax optimization, rather than as centers of cutting-edge nanoscience. Indeed, they contribute to the perception of large-scale investment in the sector, the actual return in terms of disruptive technologies and globally competitive products remains limited. This misalignment between funding appearance and outcome necessitates a more nuanced evaluation of nanotechnology’s yield. True progress in the field is inherently nonlinear and requires long-term vision. Moreover, the translational pipeline from nanoscale science to commercial technology is complex, involving multiple layers of regulation, safety, interdisciplinary integration, and market readiness.

Need of dedicated regulatory systems

Although experts and policymakers at various levels often question the output and commercial viability of nanotechnology, the

critical issue of standards and regulatory frameworks is rarely discussed and often overlooked [26]. This oversight badly hinders the broader public use of nanotechnology. Without addressing this challenge, it is impossible to envision the large-scale application of nanomaterials across technological domains. Thus, a key barrier to the commercialization of nanomaterial-based products is the absence of globally harmonized standards and coherent regulatory frameworks. A few countries actively engaged in nanotechnology have introduced nation-level regulations, but these are often not recognized internationally and may even vary across jurisdictions within the same country, mainly in federal systems. This lack of uniformity complicates cross-border commercialization and creates regulatory uncertainty for developers and industries [27]. What is especially concerning is that existing regulations are frequently adapted from frameworks originally designed for bulk materials. These are inadequate for addressing the unique physico-chemical properties, size-dependent behaviors, and long-term risks associated with nanoscale materials. As a result, scientifically appropriate, dedicated regulations for nanomaterials remain either minimal or entirely absent. This regulatory fragmentation is a global issue that badly hinders the worldwide utilization of nanotechnology. The situation is further exacerbated by the rapid pace of nanotechnology advancement, mostly in critical sectors such as healthcare, energy, agriculture, and electronics. Innovation in these fields has far outpaced the development of adequate safety, ethical, and trade-related regulations. Consequently, many companies either evade pursuing nanomaterial-based products or underreport their use to bypass complex regulatory hurdles and ensure smoother market entry.

To address these challenges, a dedicated global regulatory and standardization framework is urgently needed. This should include the establishment of an international body similar to IUPAC to develop universally accepted nomenclature, definitions, and metrological standards for nanomaterials. Such standardization would enhance scientific consistency, improve industrial classification and labeling, and support transparent communication across global supply chains. Moreover, the creation of a centralized international registry for commercially available nanoproducts is highly essential. This registry would catalog product categories, safety data, and approved applications, facilitating transparency, traceability, and coordinated post-market surveillance. A further step would be the formation of a global regulatory authority analogous to the international council for harmonization in pharmaceuticals. This body would oversee ethical deployment, standardized safety evaluations, and mutual regulatory recognition across borders. Embedding “safety by design” principles within this framework is also critical. This approach will encourage the consideration of safety

aspects from the earliest stages of product development, fostering responsible innovation. In the same line, it would reduce duplication in safety studies, streamline approval processes, and promote equitable access to safe nanotechnologies, especially in developing regions.

Probable solutions

As herein, we have pointed that instead of decades of nanotechnology research, translation from lab discoveries to societal and industrial impact remains partial. To overcome these barriers, authors suggest some constructive points: (1) Establish globally harmonized, science-driven regulatory frameworks for nanomaterials, including standardized toxicity assessment, environmental fate modeling, and lifecycle analysis to enable safe and scalable commercialization. (2) Strengthen industry engagement through public–private partnerships that integrate advanced nanomaterials such as graphene, MXenes, nanoporous catalysts, and quantum dots into manufacturable products, supported by co-funded pilot projects and shared IP models. (3) Implement strategic and transparent funding models that prioritize translational potential, incorporating techno-economic analyses, reproducibility metrics, and scalability considerations to accelerate technology readiness and safeguard industrial outcomes. (4) Address persistent misconceptions via evidence-based education and outreach, supported by interactive nanomaterial property databases, AI-driven predictive safety models, and real-time tracking of industrial applications to build public trust and informed policymaking. (5) Create standardized protocols and collaborative infrastructure through inter-laboratory validated methods, centralized pilot-scale manufacturing facilities, open-access repositories, shared instrumentation, and cloud-based simulation tools for reproducibility and scale-up. (6) Develop human capital by training engineers specialized in nanotechnology, while nurturing interdisciplinary research to drive fundamental discoveries. (7) Integration of artificial intelligence, machine learning, and digital twins can accelerate materials discovery, predict safety and performance, and guide scale-up by reducing trial-and-error paths. (8) Nanotechnology deployment must embed principles of sustainability and circular economy. Designing recyclable nanomaterials, minimizing energy-intensive synthesis, and developing green manufacturing processes will be game changers.

Conclusion

In the current era, where science is increasingly driven by commercialization, the pressure to translate fundamental research into immediate technological results has become more pronounced. However, real scientific progress is inherently incremental; it builds upon prior knowledge and often unfolds gradually over time. Nanomaterials research, like any deeply fundamental scientific domain, faces intrinsic bottlenecks, both

technical and conceptual, which cannot be overlooked. In spite of these challenges, the field is undergoing a phase of foundational maturation. Although some early-stage products and devices are marketed under the umbrella of “nanotechnology”, many of these merely represent the initial wave of applications. This phase is comparable to the early era of personal computing, such as the first-generation iPhones, technologically limited, yet instrumental in paving the way for transformative advances. Criticism directed at nanomaterial research often fails to account for this temporal reality. A common argument, echoed even by some experts, is that we are producing more PhDs than the market can absorb, with insufficient corresponding innovation and job creation. It is very true and very concerning. However, paradoxically, the same institutions and voices continue to train and graduate large numbers of doctoral students each year for vested interest. This contradiction reflects a broader systemic tension within academic and industrial research ecosystems. Nanomaterials research is now experiencing a moment not unlike that faced by other maturing scientific disciplines. Premature dismissal of the contribution of the field and excessive criticism would be a strategic and intellectual misstep. Certainly, some criticisms, largely regarding output, yield, and sustainability, have partial merit, but many stem from misconceptions, media distortion, and politically motivated narratives aimed at restricting funding for fundamental research. In reality, professionals working in nanoscience and nanotechnology continue to make steady, incremental contributions. These are critical to permitting future technological platforms in energy, healthcare, computing, and advanced manufacturing.

Acknowledgements

SKT gratefully acknowledges that the conception of this paper was inspired during the Indian Conference on Carbon Materials-2023 (ICCM-2023), held at BARC, Mumbai, where he had the privilege of serving as an invited speaker. The event brought together leading scientists and key stakeholders from the Indian government to deliberate on the impact and potential of carbon nanomaterials. The idea was further refined during the organization of the New Materials in Carbon Capture and Environmental Remediation (NMCCER 2024) conference, convened by SKT at NMAMIT, Nitte, with generous funding support from the SPARC program (Indo-UK Scheme: Project No. P3808). SKT also expresses sincere gratitude to senior professors and distinguished researchers, including the late Prof. Huzcko (Poland), Prof. Y.Q. Zhu (UK), Prof. Kuruvilla Joseph (India), Prof. Shripad T. Revankar (USA), Prof. Sung Ha (South Korea), Dr. Sukanta Das (India), and many others, for their valuable discussions during the last several years and acumens, which directly or indirectly helped shape the development of this article. SKT acknowledge his Ph.D. students, Mr.

Madhusudhana M. Devadiga and Anushree S. Bhat (NMAMIT, Nitte, India), for assistance in formatting during the preparation of the manuscript.

Funding

SKT sincerely appreciates the support of the SPARC project (P3808) under the Indo-UK scheme. Additionally, SKT extends heartfelt gratitude to Nitte (Deemed to be University) and NMAMIT, Nitte for providing the research grant (Grant No. NUFR-23-070), which has significantly facilitated our research endeavors.

Author Contributions

Santosh K. Tiwari: conceptualization; investigation; methodology; project administration; resources; supervision; validation; visualization; writing – original draft; writing – review & editing. Nannan Wang: formal analysis; software; visualization; writing – review & editing.

ORCID® iDs

Santosh K. Tiwari - <https://orcid.org/0000-0003-1602-9345>

Data Availability Statement

Data generated and analyzed during this study is available from the corresponding author upon reasonable request.

References

- Reibold, M.; Pautler, P.; Levin, A. A.; Kochmann, W.; Pätzke, N.; Meyer, D. C. *Nature* **2006**, *444*, 286. doi:10.1038/444286a
- Kokarneswaran, M.; Selvaraj, P.; Ashokan, T.; Perumal, S.; Sellappan, P.; Murugan, K. D.; Ramalingam, S.; Mohan, N.; Chandrasekaran, V. *Sci. Rep.* **2020**, *10*, 19786. doi:10.1038/s41598-020-76720-z
- Sudha, P. N.; Sangeetha, K.; Vijayalakshmi, K.; Barhoum, A. Nanomaterials History, Classification, Unique Properties, Production and Market. In *Emerging Applications of Nanoparticles and Architecture Nanostructures*; Barhoum, A.; Makhoul, A. S. H., Eds.; Micro and Nano Technologies; Elsevier: Amsterdam, Netherlands, 2018; pp 341–384. doi:10.1016/b978-0-323-51254-1.00012-9
- Charitidis, C. A.; Georgiou, P.; Koklioti, M. A.; Trompeta, A.-F.; Markakis, V. *Manuf. Rev.* **2014**, *1*, 11. doi:10.1051/mfreview/2014009
- Lu, J.; Chen, Z.; Ma, Z.; Pan, F.; Curtiss, L. A.; Amine, K. *Nat. Nanotechnol.* **2016**, *11*, 1031–1038. doi:10.1038/nnano.2016.207
- Geim, A. K.; Novoselov, K. S. *Nat. Mater.* **2007**, *6*, 183–191. doi:10.1038/nmat1849
- Tiwari, S. K.; Kumar, V.; Huczko, A.; Oraon, R.; Adhikari, A. D.; Nayak, G. C. *Crit. Rev. Solid State Mater. Sci.* **2016**, *41*, 257–317. doi:10.1080/10408436.2015.1127206
- Dresselhaus, M. S.; Dresselhaus, G.; Saito, R. *Nanotechnology* **1999**, 285–329. doi:10.1007/978-1-4612-0531-9_7
- Kong, W.; Kum, H.; Bae, S.-H.; Shim, J.; Kim, H.; Kong, L.; Meng, Y.; Wang, K.; Kim, C.; Kim, J. *Nat. Nanotechnol.* **2019**, *14*, 927–938. doi:10.1038/s41565-019-0555-2
- Xiao, X.; Yu, H.; Jin, H.; Wu, M.; Fang, Y.; Sun, J.; Hu, Z.; Li, T.; Wu, J.; Huang, L.; Gogotsi, Y.; Zhou, J. *ACS Nano* **2017**, *11*, 2180–2186. doi:10.1021/acsnano.6b08534
- Ares, P.; Novoselov, K. S. *Nano Mater. Sci.* **2022**, *4*, 3–9. doi:10.1016/j.nanoms.2021.05.002
- Binns, C. *Introduction to Nanoscience and Nanotechnology*; John Wiley & Sons: Hoboken, NJ, USA, 2021. doi:10.1002/9780470618837
- Khatoun, U. T.; Velidandi, A. *Sustainability* **2025**, *17*, 1250. doi:10.3390/su17031250
- Chemistry World | March 2011 | Nanotech decade. https://www.rsc.org/images/Nanotechnology%20-%20Nanotech%20Decade_tcm18-198617.pdf#page=2.59 (accessed Nov 18, 2025). doi:10.1021/cs200652y
- Rambaran, T.; Schirhagl, R. *Nanoscale Adv.* **2022**, *4*, 3664–3675. doi:10.1039/d2na00439a
- Son, S.; Min, H. S.; You, D. G.; Kim, B. S.; Kwon, I. C. *Nano Today* **2014**, *9*, 525–540. doi:10.1016/j.nantod.2014.06.002
- Malloy, T. F. *ACS Nano* **2011**, *5*, 5–12. doi:10.1021/nn103480e
- Zhou, H.; Lee, T.-W. *IEEE Spectrum* **2020**, *57*, 24–29. doi:10.1109/mspec.2020.9262146
- Luo, Z.; Manders, J.; Yurek, J. *IEEE Spectrum* **2018**, *55*, 28–53. doi:10.1109/mspec.2018.8302384
- Mom, G.; Kirsch, D. A. *Technol. Cult.* **2001**, *42*, 489–518. doi:10.1353/tech.2001.0128
- Li, M.-C.; Liu, X.; Lv, K.; Sun, J.; Dai, C.; Liao, B.; Liu, C.; Mei, C.; Wu, Q.; Hubbe, M. *Prog. Mater. Sci.* **2023**, *139*, 101187. doi:10.1016/j.pmatsci.2023.101187
- Giese, B.; Klaessig, F.; Park, B.; Kaegi, R.; Steinfeldt, M.; Wigger, H.; von Gleich, A.; Gottschalk, F. *Sci. Rep.* **2018**, *8*, 1565. doi:10.1038/s41598-018-19275-4
- Phan, H. T.; Haes, A. J. J. *Phys. Chem. C* **2019**, *123*, 16495–16507. doi:10.1021/acs.jpcc.9b00913
- Pietrojusti, A.; Stockmann-Juvala, H.; Lucaroni, F.; Savolainen, K. *Wiley Interdiscip. Rev.: Nanomed. Nanobiotechnol.* **2018**, *10*, e1513. doi:10.1002/wnan.1513
- Maslej, N.; Fattorini, L.; Perrault, R.; Gil, Y.; Parli, V.; Kariuki, N.; Capstick, E.; Reuel, A.; Brynjolfsson, E.; Etchemendy, J.; Ligett, K.; Lyons, T.; Manyika, J.; Niebles, J. C.; Shoham, Y.; Wald, R.; Walsh, T.; Hamrah, A.; Santarlasci, L.; Lotufo, J. B.; Rome, A.; Shi, A.; Oak, S. *arXiv* **2025**, 2504.07139. doi:10.48550/arxiv.2504.07139
- Miernicki, M.; Hofmann, T.; Eisenberger, I.; von der Kammer, F.; Praetorius, A. *Nat. Nanotechnol.* **2019**, *14*, 208–216. doi:10.1038/s41565-019-0396-z
- Allan, J.; Belz, S.; Hoeveler, A.; Hugas, M.; Okuda, H.; Patri, A.; Rauscher, H.; Silva, P.; Slikker, W.; Sokull-Kluettgen, B.; Tong, W.; Anklam, E. *Regul. Toxicol. Pharmacol.* **2021**, *122*, 104885. doi:10.1016/j.yrtph.2021.104885

License and Terms

This is an open access article licensed under the terms of the Beilstein-Institut Open Access License Agreement (<https://www.beilstein-journals.org/bjnano/terms>), which is identical to the Creative Commons Attribution 4.0 International License (<https://creativecommons.org/licenses/by/4.0>). The reuse of material under this license requires that the author(s), source and license are credited. Third-party material in this article could be subject to other licenses (typically indicated in the credit line), and in this case, users are required to obtain permission from the license holder to reuse the material.

The definitive version of this article is the electronic one which can be found at:
<https://doi.org/10.3762/bjnano.16.149>